www.elsevier.com/locate/yjtbi

Rapid Simulation of Spatial Epidemics: A Spectral Method

Samuel P.C. Brand, Michael J. Tildesley, Matthew J. Keeling

PII: S0022-5193(15)00036-3
DOI: http://dx.doi.org/10.1016/j.jtbi.2015.01.027
Reference: YJTBI8055

To appear in: *Journal of Theoretical Biology*

Received date: 19 August 2014
Revised date: 15 January 2015
Accepted date: 26 January 2015

Cite this article as: Samuel P.C. Brand, Michael J. Tildesley, Matthew J. Keeling, Rapid Simulation of Spatial Epidemics: A Spectral Method, *Journal of Theoretical Biology,* http://dx.doi.org/10.1016/j.jtbi.2015.01.027

Rapid Simulation of Spatial Epidemics: A Spectral Method

Samuel P. C. Brand[ac], Michael J. Tildesley[b], Matthew J. Keeling[ab]

Abstract

Spatial structure and hence the spatial position of host populations plays a vital role in the spread of infection. In the majority of situations, it is only possible to predict the spatial spread of infection using simulation models, which can be computationally demanding especially for large population sizes. Here we develop an approximation method that vastly reduces this computational burden. We assume that the transmission rates between individuals or subpopulations are determined by a spatial transmission kernel. This kernel is assumed to be isotropic, such that the transmission rate is simply a function of the distance between susceptible and infectious individuals; as such this provides the ideal mechanism for modelling localised transmission in a spatial environment. We show that the spatial force of infection acting on all susceptibles can be represented as a spatial convolution between the transmission kernel and a spatially extended 'image' of the infection state. This representation allows the rapid calculation of stochastic rates of infection using fast-Fourier transform (FFT) routines, which greatly improves the computational efficiency of spatial simulations. We demonstrate the efficiency and accuracy of this *fast spectral rate recalculation* (FSR) method with two examples: an idealised scenario simulating an SIR-type epidemic outbreak amongst N habitats distributed across a two-dimensional plane; the spread of infection between US cattle farms, illustrating that the FSR method makes continental-scale outbreak forecasting feasible with desktop processing power. The latter model demonstrates which areas of the US are at consistently high risk for cattle-infections, although predictions of epidemic size are highly dependent on assumptions about the tail of the transmission kernel.

[a]Department of Life Sciences, University of Warwick, Gibbet Hill Rd, Coventry, CV4 7AL
[b]Mathematics Institute, University of Warwick, Gibbet Hill Rd, Coventry, CV4 7AL
[c]Corresponding author, S.Brand@warwick.ac.uk +447899986842

Highlights

- Kernel-based spatial transmission models are computationally expensive for large population sizes.
- We present an efficient and accurate alternative simulation methodology (dubbed FSR simulation) based upon a spectral representation of the infection rate.
- FSR simulation also permits the accelerated likelihood calculation for more efficient parameter inference.
- Using FSR simulation it was possible to perform detailed outbreak forecasting for a generic cattle infection at the continental-scale.

Keywords

Accelerated simulation, Epidemics, Cattle infections.

1. Introduction

Understanding the dynamics of infection invading a spatially structured population is of both theoretical interest and practical importance. The theoretical interest is due to the impact of relaxing the homogenous mixing assumption common to classical models of epidemic dynamics. The main practical concern is the effect that the introduction of heterogeneity in population mixing has on key model predictions, such as the rate of recruitment of new infecteds [1], the spatial variation of infection risk [2] and in particular the consequences of targeted control measures [3, 4]. In contrast to other forms of population heterogeneity in epidemic models (such as age-structure), spatial structuring focuses attention on the location of the initial infectious seeds and the ensuing dynamics of invasion often characterised by a travelling spatial wave. The emergent spatio-temporal patterns of infection are dominated by this invasion mechanism, with epidemic risk to the underlying population being due to environmental factors such as habitat location and aggregation of individuals.

There are several approaches to modelling the dynamics of the spread of spatial infection, including PDE models [5], agent-based models [6], and models based on an underlying contact network [7], but the metapopulation model is often the preferred formulation due to its relative simplicity and flexibility. The metapopulation model consists of a set of discrete point habitats in continuous space, each with its own internal dynamics, which can interact with each other. Its origins date back over 40 years [8], but it is experiencing increasing use in a wide number of problems in population dynamics [9, 10]. While the original metapopulation model assumed an equal rate of interaction between all habitats, the inclusion of more realistic rates that depend on spatial separation has lead to a greater understanding of the roles of spatial structure, with applications in as diverse settings as population biology [11, 12], conservation biology [13], evolutionary biology [14] and epidemiology [15, 16, 17].

In rejecting spatially homogeneous models it has become common to include the rate of transmission between two spatial locations as a distance varying spatial transmission kernel, even for models with considerable implications for public policy, such as predictive modelling for Foot-and-mouth intervention strategies [18, 19]. The transmission kernel can be naturally interpreted as an unnormalised dispersal distribution for 'offspring' from their originating infectious 'parent', combining the rate of 'offspring' production, transmissibility/survivability of the 'offspring' and the spatial distribution of it's dispersed location. This interpretation essentially unifies spatial invasion models of both species [20] and epidemics [21]. The 'offspring' of an infectious source being interpreted as potential infectious contacts in the epidemic model. When the entire background space is uniformly available there are distinct phenomenological differences between kernel-based models where transmission rate decays exponentially with distance (or faster) and those with slower, 'heavy-tailed' transmission rate decay. Essentially 'light-tailed' kernels lead to an asymptotic invasion front expanding with a certain velocity whereas 'heavy-tailed' kernels lead to a continuously accelerating patchy invasion. This phenomenological dependence on kernel tail decay for models with homogeneously distributed hosts has been confirmed by both analysis [22] and simulation [23]. For the metapopulation model used in this work analysis will be considerably complicated by heterogeneous distributions of potential host populations for the infectious pathogen and heterogeneous demogra-

phy from population to population. In this more realistic situation Monte Carlo (MC) simulation becomes the main approach for investigating the expected outcomes of epidemic outbreak, although one might expect transmission kernel tail decay to play an important role in analogy to the stronger results for simpler models outlined above.

Simulation is a universally applicable approach to investigating these metapopulation models, allowing flexibility in adding further realism to the general model framework. If scientific or statistical confidence in the relevant parameters can be achieved, then MC simulation methods can have 'real-world' predictive power [24]. However, for stochastic simulation the MC convergence of the observables of interest can require a very large number of independent replicates of simulated epidemic realisations. Moreover, this problem is compounded whenever insight requires the sweeping of large regions of plausible parameter space, or when the results of simulation are required for parameter inference, e.g. when using an approximate bayesian computation (ABC) method [25, 26, 27]. The requirement to perform very many independent realisations puts great emphasis on the development of highly efficient algorithms for stochastic simulation, even at the cost of mild inexactness (an example of such an approach is [28]).

The essential non-linearity in epidemic models is due to the interaction between susceptible and infectious individuals. In this spatial metapopulation context each susceptible habitat becomes infected due to the summed risk of transmission from all infectious habitats. Therefore, naively a simulation must calculate (and sum) the transmission strength between all susceptible - infectious pairs in the population; and this value must be recalculated after any event that changes the infection status of the population. Since the number of possible pairs grows quadratically with the number of individuals, it is this calculation that becomes the main bottleneck for stochastic spatial simulation, and it is improving the efficiency of this calculation that is the subject of this paper.

Here we present the fast spectral rate recalculation (FSR) method for simulating spatial epidemics this utilises a rapid estimation of the force of infection rather than calculating the sum over infected habitats directly. Inspired by Galerkin methods common to the numerical investigation of

PDEs [29], this approach is motivated by representing the force of infection as a smooth field over all space. After approximating the habitat locations as unit mass Gaussian distributions in space, the spectral projection of this force of infection field onto a regular grid of size M can be calculated efficiently using FFT (Fast Fourier Transform) at a computational cost of $\mathcal{O}(M \ln M)$. The infection rate for each susceptible habitat can then be determined by interpolation on nearest grid points. This compares favourably with the potentially $\mathcal{O}(N^2)$ cost of calculating the infection rate for all susceptibles from the direct definition in a population of size N. We will demonstrate that although this methodology is an approximate scheme, the error due to the spectral projection can be made negligible by decreasing grid separations (increasing M). For large numbers of habitats, where the transmission kernel is relatively wide (that is many infectious habitats contribute to the risk of infection for each susceptible habitat) the spectral method can be implemented with low error whilst still retaining substantial speed advantage over simulations using direct summation to calculate force of infection. Finally we will present two examples to illustrate the potential usefulness of the FSR method. Firstly, using a simple spatial SIR model, that FSR methodology can be adapted in a straightforward manner to accelerate likelihood based inference for spatial epidemic processes with negligible loss in accuracy. Secondly, a simulation-based case study of outbreak predictions for a disease spreading amongst US cattle farms based upon agricultural census data and under varying assumptions about range and intensity of farm to farm transmission. The much greater numerical efficiency of the FSR method was crucial for making a continent-scale epidemiological study feasible despite using only desktop computing power.

2. Methods

The basic methodology is introduced in stages; firstly the basic spatial model framework and state space of the model are defined. We then describe existing methods for simulating the dynamics of infection before showing how the force of infection on a habitat can be represented as a convolution on the spatial locations. This leads to a novel algorithm (termed the Fast Spectral Rate or FSR) to simulate spatial epidemics. Later in the results section we focus on the accuracy and computational efficiency of this new algorithm.

2.1. Spatial Risk of Transmission

In this work we consider modelling the spread of a infectious disease within a population spatially segregated between N indexed habitats each with a location co-ordinate $(x_i)_{i=1}^N$ in two dimensions. Each habitat is considered to be inhabited by a single host individual described by some discrete disease state, and therefore the model conforms to the standard Levins-type metapopulation [8]. (In principle the methodology outlined here readily extends to stochastic populations at each habitat, but the single host assumption makes the formulation more transparent.) Additionally, each habitat is treated as sufficiently small compared to the background space that it can be modelled as a point location. We are concerned with spatial transmission of the disease; hence we replace the Levins state alphabet of 'not occupied' or 'occupied' with 'Susceptible' (S) and 'Infected and Infectious' (I). Depending on the characteristics of the disease the state alphabet may be augmented to reflect the underlying epidemiology, such as including a 'Removed' (R) class denoting those habitats where after a period spent infectious the habitat ceases to play a further role in the epidemic. In this work we will concentrate on epidemic models where each habitat that becomes infected will eventually be removed, conforming to the standard SIR paradigm.

The underlying epidemic is treated as a random process, where it is useful to describe the state of each habitat i using the boolean-valued disease state indicators, $S_i(t), I_i(t)$, as well as additional indicator representing additional model complexity, e.g. $R_i(t)$. Hence $S_i(t)$ takes the value one if the individual in habitat i is susceptible at time t, or zero otherwise. The rate at which an infectious (I) habitat j transmits to a susceptible (S) habitat i is governed by a spatial transmission kernel K, which we assume depends only on the (Euclidean) distance between the two habitats e.g. $K(x_i, x_j) \equiv K(|x_i - x_j|)$. (Note that this assumption restricts us to considering translational invariant kernels, such that the precise locations of the habitats are irrelevant and transmission only depends on their relative positions). Hence, the *force of infection* on habitat i is,

$$\lambda_i(t) = \sum_{j=1}^{N} K(x_i - x_j) I_j(t). \tag{1}$$

For continuous time models the probabilistic dynamics of the infection process for each habitat i is,

$$\mathbb{P}(\text{Infection event at habitat } i \in [t, t+\delta t]) \quad = \quad S_i(t)\lambda_i(t)\delta t + o(\delta t). \tag{2}$$

The above holding for arbitrary $\delta t > 0$.

In this paper however we will be mainly concerned with related discrete time processes. This can either be viewed as an approximation to the continuous time process or an independent model in its own right where the epidemic processes occur on a natural cycle (e.g. daily). For many natural systems there is a clear daily cycle, and host behaviour and therefore transmission rates may vary substantially between day and night time; in such cases a discrete time model may be viewed as more realistic than a continuous (time homogeneous) model. In this discrete time model infection and recovery events do not have instantaneous effect on the stochastic rates of all other events but impact on the subsequent time step. Having chosen the cycle period $\delta t^* > 0$ as a model choice, we can derive the following discrete time dynamics from (2) using the assumption of periodically updating states, arriving at the Keeling-type [18] model

$$\mathbb{P}(\text{Inf. event at susceptible habitat } i \in [t_n, t_{n+1}] \mid S_i(t) = 1) \quad = \quad 1 - \exp(-\lambda_i(t_n)\,\delta t^*), \tag{3}$$

where $t_n = n(\delta t^*), n \in \mathbb{N}$. For practical purposes the cycle period δt^* can be absorbed into the parameterisation of the discrete time epidemic model by treating $\delta t^* = 1$ and varying the remaining parameters.

Rather than simulate infection events directly from (3) it is convenient and more efficient to use an equivalent discrete time Sellke construction [30]. Each habitat i is assigned a random epidemic resistance $Z_i \sim \exp(1)$ and at each time step accumulates infectious pressure Λ_i according to its force of infection,

$$\Lambda_i(t) = \Lambda_i(t-1) + \lambda_i(t) = \sum_{s=0}^{t} \lambda_i(s) \qquad t = 0, 1, 2 \ldots. \tag{4}$$

The habitat i becomes infected on the first time step that $\Lambda_i(t) > Z_i$. The computational advantage of the Sellke construction is that resistances $\{Z_i\}_{i=1}^N$ can be pre-generated before a simulation run, since they are independent of the dynamics, as can other random periods such as the infection duration of each habitat. Altogether, these pre-generated random numbers encode the full stochastic dynamics of a spatial epidemic realisation; we follow Cook et al [31] in referring to them as the *latent variables*, Z, of the epidemic. We will utilise latent variable matching in order to compare epidemic realisations using to direct calculation of the force of infection $\lambda_i(t)$ to those using the FSR approximation.

2.2. The Force of Infection as a Spatial Convolution

After an initial early growth period a successfully invasive pathogen will typically infect a significant ($\mathcal{O}(N)$) number habitats during the course of an epidemic. For simulations where a large number of habitats are under consideration, the necessary recalculation of the force of infection, $\lambda_i(t)$, for each susceptible habitat after each time-step therefore becomes computationally burdensome. A brute force approach to this task requires a sum over all infected habitats for each susceptible habitat at a computational cost of $\mathcal{O}(N^2)$ per time-step. An immediate saving is made by including $\{\lambda_i(t)\}_{i\in S}$ as part of the epidemic state, updating (rather than recalculating) for each susceptible habitat upon each event. Hence, for E events occurring in a time-step, the force of infection recalculation is of cost $\mathcal{O}(EN)$. We call this approach *stochastic simulation with rate updating*. For simulation of the discrete time model (3) the recalculation still scales as $\mathcal{O}(N^2)$, due to the fact that $E \sim \mathcal{O}(N)$, although there is a significant saving compared to full recalculation.

We propose a method of accelerating stochastic simulation by reducing the computational burden involved in recalculation of the force of infection for each susceptible habitat after E events have occurred in a time-step of our simulation method. The basic idea is to treat $\lambda_i(t)$ as a single point of a continuous field, which is derived from a convolution between the transmission kernel and a spatial distribution of infected habitats. This field is calculated on a set of M grid points, making use of the observation that a convolution maps to a simple product when a Fourier transform is

taken. The computational effort of convolution solving using FFT (Fast Fourier Transform) on M collocation points grows $\mathcal{O}(M \log M)$, which is potentially very efficient compared to brute force calculation of the force of infection. We follow the formalism of Ovaskainen and Cornell [11, 12] in representing the spatial spread of the infection across the habitats as a weighted sum of delta distributions. We call this the spatially extended *image* of the infectious sources,

$$f_I(x,t) = \sum_{i=1}^{N} \delta(x - x_i) I_i(t), \qquad x \in \mathbb{R}^2. \tag{5}$$

In a similar manner, the force of infection is extended to a field *for every point in* $\mathbb{R}^2$. This field has the compact expression as a convolution

$$\begin{aligned} \lambda(x,t) &= \sum_{j=1}^{N} K(x - x_j) I_j(t) \\ &= \sum_{j=1}^{N} \int K(x - y) \delta(y - x_j) I_j(t) dy \\ &= (K * f_I)(x,t), \end{aligned} \tag{6}$$

here, $*$ represents convolution over the spatial variables, $(f * g)(x,t) = \int f(x-y,t) g(y,t) dy$. For a given epidemic state, $X(t)$, the force of infection at each habitat i is recovered through the identity $\lambda_i(t) = \lambda(x_i, t)$.

The conceptual power behind our approach is to use this convolution representation to rapidly calculate the force of infection field λ on M collocation points and use local interpolation to estimate λ_i (for all susceptibles) at each time-step of the stochastic integration scheme.

2.3. Fast Spectral Rate Recalculation

Our goal is to reduce the problem of simulating stochastic epidemic dynamics in continuous space to a closely approximated problem on a discrete grid. The grid-based dynamics can be simulated much more efficiently than the full system dynamics using FFT techniques, since the force of infection on each habitat can be rapidly recalculated after infection or recovery events. The use of FFT requires periodic boundary conditions for I_l, and in this section we maintain this assumption;

Parameter/Function	Definition
$\{x_i\}_{i=1}^N$	Habitat locations
K	Spatial Transmission kernel
K'	Transformed Spatial Transmission kernel
λ_i	Force of infection, Habitat i
f_I	Image of infection
ϵ	Width of Gaussian Approximation
Δx	Separations in collocation grid
f_I^ϵ	Blurry Image of infection
λ	Force of infection field
$\Phi_{\Delta x}^l$	Approximation grid
$\lambda_{PS}^{M,\epsilon}$	FFT estimated Force of infection field

Table 1: Model Parameters and Functions

in the following section we consider how this assumption can be relaxed.

Two ideas underpin accelerating the calculation of the force of infection (Figure 1). Firstly, the image of the infectious sources is 'blurred' by approximating each delta distribution as a Gaussian shaped function of width $\epsilon > 0$; this is so that infection potential can be approximated as originating from grid points. For real populations where individuals are not tied to a point location, this Gaussian blurring may actually more closely reflect reality. Secondly, we solve an analogous equation to (6) defined on a discrete collocation grid using efficient FFT convolution solving and read off $\{\lambda_i(t)\}_{i=1}^N$ directly from a local interpolation scheme.

To this end we introduce a 2-dimensional regular grid over an $l \times l$ area, with a spacing Δx between grids,

$$\Phi_{\Delta x}^l = \{\boldsymbol{i} = \Delta x(i_1, i_2) \mid (i_1, i_2) \in \mathbb{Z}^2,\ \boldsymbol{i} \in I_l\}. \tag{7}$$

These grid-points are the *collocation* points used for the discrete transformation, that is the points at which the force of infection is calculated. By varying the spacing Δx we can use M collocation points to cover our space, however we always choose Δx such that $l/\Delta x = m \in \mathbb{N}$, leading to $M = m^2$. A full list of parameters used is given in table 1.

Since our goal is to utilise the efficiency of FFT algorithms we require that both the transmission kernel and image of infection can be well approximated by their support on the collocation grid. This will not be true for the delta distributions in the definition of f_I since they are not functions in the traditional sense, but rather distributions in a more general sense [32]. We resolve this problem by introducing the *blurred image of infection*, f_I^ϵ, where the delta distributions in the image definition (5) are replaced by tight Gaussians of width ϵ (> 0),

$$f_I^\epsilon(x,t) = \sum_{i=1}^{N} \delta_\epsilon(x - x_i) I_i(t), \qquad \delta_\epsilon(x) = \frac{1}{2\pi\epsilon^2} e^{-\frac{-|x|^2}{2\epsilon^2}}. \tag{8}$$

To provide even greater computational efficiency, we treat these Gaussians as having finite range, cutting off at a distance of 5ϵ. The number of collocation points local to habitat i (that are involved with the blurring of the image of i) is denoted $n_i = |\{\boldsymbol{i} \in \Phi^l_{\Delta x} \; s.t. \; |\boldsymbol{i} - x_i| < 5\epsilon\}|$.

The natural grid-based approximation to the integral form of the force of infection field (6) on the periodic domain I_l is to use a sum over grid points, respecting the periodic boundary conditions,

$$\lambda(\boldsymbol{i}, t) \approx (\Delta x)^2 \sum_{\boldsymbol{j} \in \Phi^l_{\Delta x}} K(\{\boldsymbol{i} - \boldsymbol{j}\}_l) f_I^\epsilon(\boldsymbol{j}, t), \tag{9}$$

where $\{\boldsymbol{i} - \boldsymbol{j}\}_l$ represents periodic summation of all distances between $\boldsymbol{i}$ and $\boldsymbol{j}$ on a periodic domain, although in our examples only the shortest vector between points $\boldsymbol{i}$ and $\boldsymbol{j}$ on the periodic space I_l will contribute. The approximation (9) is in the form of a circular convolution sum which can be efficiently solved (see supporting information) using Fourier (FFT) coefficients of the transmission kernel ($\tilde{K}$) and the blurry image of infection ($\tilde{f}_I^\epsilon$) and the inverse fast Fourier transform (IFFT) operation $F^{-1}[\cdot]$,

$$\lambda(\boldsymbol{i}, t) \;\; \approx \;\; \lambda_{PS}^{M,\epsilon}(\boldsymbol{i}, t) = (\Delta x)^2 F^{-1}[\tilde{K} \tilde{f}_I^\epsilon](\boldsymbol{i}, t), \tag{10}$$

where $\lambda_{PS}^{M,\epsilon}$ is equivalently the exact solution to the sum (9) and the discrete Fourier transform, or pseudo-spectral, approximation to the force of infection field with Gaussian blurring; the computa-

tional burden for its solution everywhere on the grid grows as $\mathcal{O}(M \ln M)$. Once, we have estimated the force of infection on the grid of points, $\Phi^l_{\Delta x}$, we can read off an approximation for $\lambda_i(t)$ from local bilinear interpolation from the 4 grid points nearest x_i.

The relationship between the Fourier pseudo-spectra of the 'true and 'blurry' images of infection is approximately

$$\tilde{f}^\epsilon_I(\omega, t) \approx \tilde{\delta}_\epsilon \tilde{f}_I(\omega, t), \qquad \omega \in \mathbb{Z}^2, \tag{11}$$

where δ_ϵ is the zero centred Gaussian (8) and ω is a discrete wavenumber for the pseudo-spectrum. Equation (11) motivates defining a *transformed kernel spectrum* $\tilde{K}'$,

$$\tilde{K}'(\omega) = \frac{\tilde{K}(\omega)}{\tilde{\delta}_\epsilon(\omega)}, \qquad \omega \in \mathbb{Z}^2. \tag{12}$$

The approach being to as far as possible reduce the error due to using Gaussian approximations of delta functions whilst retaining their numerical convenience. Numerical investigation suggests that using the transformed kernel spectrum (12) improves the accuracy of the pseudo-spectral approximation to the force of infection field compared to using the discrete spectrum $\tilde{K}$ directly (see supporting information). A secondary benefit of using the transformed kernel spectrum is to largely eliminate ϵ dependence from parameterisation of the FSR simulation scheme. Throughout we choose ϵ sufficiently great so that the mass of the Gaussians (8) is fully supported on the grid ($\tilde{\delta}_\epsilon(0) \approx 1$) but no greater. A detailed error analysis reveals that, without kernel spectrum transformation, the accuracy of the FSR method depends more strongly upon ϵ with both extremes $\epsilon \ll \Delta x$ and $\epsilon \gg \Delta x$ being poor parameter value ranges. We refer the reader to the supporting information.

We call simulation using recalculation of $\lambda^{M,\epsilon}_{PS}$ and local interpolation the *fast spectral rate recalculation* (FSR) method, and can be represented by the following algorithm.

Fast Spectral Rate Recalculation (FSR) algorithm:

1. Choose a suitable FFT algorithm and number of simulation repetitions.
2. Perform one-off pre-calculations:
   (a) Calculate and store local points for each habitat i, $\{\boldsymbol{i} \in \Phi^l_{\Delta x} \; s.t. \; |\boldsymbol{i} - x_i| < 5\epsilon\}$.
   (b) Calculate pseudo-spectra of transmission kernel $\tilde{K}$, zero-centred Gaussian $\tilde{\delta}_\epsilon$ and transformed kernel $\tilde{K}'$, avoiding zero division error in (12).
3. Choose initial epidemic state, construct the initial blurry image of infection $f^\epsilon_I(\boldsymbol{i}, 0)$, and set $t = 0$.
4. Solve the sum $\lambda^{M,\epsilon}_{PS}(\boldsymbol{i}, t)$, $\forall \boldsymbol{i} \in \Phi^l_{\Delta x}$, by using an FFT algorithm to construct the product function $\tilde{K}\tilde{f}_I$ and taking IFFT using transformed kernel, $F^{-1}[\tilde{K}'\tilde{f}_I]$.
5. Re-normalise $\lambda^{M,\epsilon}_{PS}$ by the factor $(\Delta x)^2$, if this is not performed by the FFT algorithm.
6. Perform stochastic time-step update using rates of infection $\lambda_i(t)$ read off from bi-linear interpolation of $\lambda^{M,\epsilon}_{PS}(\boldsymbol{i}, t)$.
7. For each of E events that occurred in step 6., update f^ϵ_I on $\Phi^l_{\Delta x}$ at the n_i local points to the habitat where the event has occurred.
8. If there are remaining infected habitats set $t \to t+1$ and return to 4. If epidemic has finished, stop simulation.
9. If further simulations are required return to 3. The information calculated in 2. can be reused.

Conveniently, there are a multiplicity of high quality FFT algorithms publicly accessible, for example the FFTw library for C programming or the high quality FFT routine in MATLAB. Hence, there is no necessity for the reader to construct their own transformation algorithm. The convergence and error analysis of random epidemics generated using FSR method onto the 'true' random epidemic defined by dynamics such as (3) is discussed in supporting information.

Although we have chosen to illustrate the use of the FSR method with the motivating example of the spatial SIR-type epidemic, it should be noted that this methodology holds for any type of stochastic spatial process where the stochastic rate for events can be written in the form (6). Examples therefore include a range of spatial epidemiological models (eg SEIR-type and SIS-type dynamics) and spatial ecological models where a local interaction process governs competition or colonisation. In particular, the necessary ingredients for using FSR are,

- (Euclidean) Spatially distributed individuals or densities,
- Smooth and translation invariant spatial interactions.

2.3.1. Non-periodic Boundary Conditions

In many real-world applications the idealised periodic boundary conditions are unrealistic: physical boundaries to transmission may play an important role in containing epidemic spread, or the habitats may exist in a finite domain isolated from external infection. However, FSR implicitly requires periodic boundary conditions in solving the convolution sum (10); essentially modelling the dynamics on a torus rather than a finite plane. To circumvent this problem and yet retain the efficiency of using FFT we embed our original space, I_l, within a larger extended space, $I_{l'}$, setting $l' > l$ sufficiently large such that $l'-$periodic extensions of λ do not interact. This is done by placing the habitats in the smaller space I_l, and then subsequently creating an empty padded space for f_I^ϵ on $I_{l'}$. On this larger space an infection event has a zero probability of 'wrapping' round the space $I_{l'}$. We achieve this either by restricting to transmission kernels of compact support, or by imposing compact support by finite range truncation. We therefore set the epidemic on $I_{l'}$ and use the FSR method for fast calculation of $\lambda(\boldsymbol{i}, t)$ on $\boldsymbol{i} \in \Phi_{\Delta x}^{l'}$ as above.

3. Results

We present results and analyse the accelerated performance due to using the FSR method for a spatially distributed population of varying size undergoing an SIR-type epidemic. The deviation between epidemic simulation using direct rate recalculation and simulation using the FSR method was firstly investigated by comparing their resultant epidemic curves and spatio-temporal distribution of infected habitats at epidemic peak. More systematically error between direct and FSR simulation was measured using latent variable matching in the sense of Cook et al [31]; essentially the latent random variables encode the intrinsic stochastic fluctuations of the spatial epidemic process and therefore deviation between epidemics with identical latent variables is due solely to error in the rate calculation. By choosing sufficiently fine grid spacing (small Δx) it was found that FSR simulation could be highly accurate even whilst delivering significant time saving per replicate. The time saving due to using the FSR method became relatively more favourable compared

to direct simulation as the population size N became larger. We also demonstrate the possibility of using FSR rate calculation to accelerate likelihood-based parameter inference for this class of spatial epidemic model. Finally, we present a FSR-simulation case study of continental-scale epidemic outbreak amongst commercial US cattle farms, using spatial data that accurately reflect US agricultural census data at the county scale. Effects of farm size on the epidemic dynamics are introduced without compromising the numerical efficiency of the FSR method.

3.1. Epidemic Spread amongst a Spatial Metapopulation

For the examples in this section the habitat locations are given within a $l \times l$ square in two dimensional space ($\{x_i\}_{i=1}^N \in [-l/2, l/2]^2 = I_l \subset \mathbb{R}^2$). For simplicity we consider a discrete time spatial epidemic model conforming to the classic SIR paradigm, such that infected individuals recover and are then immune. Discrete time steps are chosen to reflect a daily change in disease status with all rates given in units of $(\text{days})^{-1}$, and therefore the time scale $\delta t^* = 1$ day. In addition to the stochastic infection dynamics (3) there are the additional recovery dynamics; for each infectious habitat (individual) i the daily probability of removal/recovery is,

$$\mathbb{P}(\text{Rec. event at hab. } i \mid I_i(t) = 1) \;\; = \;\; 1 - \exp(-\gamma). \tag{13}$$

Where the recovery rate $\gamma = 0.1$ $(\text{days})^{-1}$ is used in this section; this gives an average infectious duration of 10.5 days given the discrete nature of the time-steps. The habitat location coordinates were chosen as independent spatial Poisson points on I_l. The length scales are fixed by choosing units such that the habitat density $N/l^2 = 1$. The length scale of transmission, L, is given in these units. For each N considered, the random distribution of habitat locations was realised once, with further simulations performed on identical landscapes. Non-periodic boundary conditions as described above were imposed to replicate the fixed spatial scale of the population.

The transmission kernel $K(x, y)$ encodes the rate of potentially infectious contact from an infectious source at some point x to point y. However, in this work we only consider radially symmetric kernels; that is $K(x, y) = K(x', y')$ whenever $|x - y| = |x' - y'|$. This is most naturally expressed in polar co-ordinates and we also use $K(r)$ to denote the rate of transmission between two points at

range r; in two spatial dimensions the total potentially infectious contact rate in the infinitesimal range interval [r,r+dr) is $2\pi r K(r)dr$. Treating the radially symmetric transmission kernel as an (unnormalised) spatial density gives three natural summary statistics, independent of the distribution of susceptibles: the magnitude of the kernel, the mean range of dispersal and the variance in the range of dispersal.

$$\text{Magnitude}(K) = 2\pi \int_0^\infty rK(r)dr, \tag{14}$$

$$\text{Mean}(K) = \frac{\int_0^\infty r^2 K(r)dr}{\int_0^\infty rK(r)dr}, \tag{15}$$

$$\text{Var}(K) = \frac{\int_0^\infty r^3 K(r)dr}{\int_0^\infty rK(r)dr} - \text{Mean}(K)^2. \tag{16}$$

In the idealised scenario of a uniformly distributed population of susceptibles the summary statistics define the actual rate of infection and range statistics of successful infections.

The transmission kernel for this section was chosen from the family of Gaussian shaped functions with width L, $\{K(\cdot; L)\}_{L>0}$ such that

$$K(|x|; L) = \frac{\beta}{2\pi L^2} e^{-|x|^2/2L^2}. \tag{17}$$

For $l \gg L$, β sets the magnitude of the transmission kernel over I_l independently of length scale L. The mean and variance of dispersal for the Gaussian kernel in two dimensions are $\text{mean}(K) = \sqrt{\pi/2}L$ and $\text{Var}(K) = (2-\pi/2)L^2$. This directly links the length scale parameter L to the expected range of dispersal of infected habitats. As a reference, in the limit $L \to \infty$ spatial position becomes irrelevant and the epidemics collapses into the well understood non-spatial or mean-field stochastic SIR model with population size N [1, 33] albeit in discrete time. We choose $\beta = 0.2$ (days)$^{-1}$, where the pathogen can successfully invade except at small values of L.

3.1.1. Performance of FSR method compared to direct simulation

We took as default parameters a metapopulation of $N = 12,100$ habitats in a 110×110 box, with $\beta = 0.2$, $L = 3$ defining the Gaussian shaped transmission kernel. We stress that this relatively

localised transmission kernel (relative to the scale of the system and the density of habitats) places a severe test on the FSR methodology. The FSR method was implemented using a collocation grid of size $M = 256^2$, which gave a grid separation $\Delta x = 0.5$ on an augmented box of side length $110 + 6L$ used in order to implement non-periodic boundary conditions. Habitat point locations were approximated as Gaussians of width $\epsilon = 0.4$. To initiate the epidemic, a single infected source farm was positioned in the centre of the box and the 9 closest habitats where also infected.

Simulation, using direct rate calculation with 1000 replicates, indicated that epidemic realisations typically recruit locally to the origin before an invasion front formed, infection then spreading in a wave-like manner throughout the space causing a declining epidemic tail due to exhaustion of available susceptible habitats. FSR simulation captured this phenomenology and closely replicated the expected dynamics observed with direct simulation, including the expected peak day ($t_{peak} = 134$ days). The maximum absolute deviation in expected number of infecteds between the methods, $\sup_{t\geq 0}\{|\langle \mathbb{E}[(I_{FSR} - I_{dir})(t)]\rangle|\} = 16.85$ habitats, was small compared to the size of the metapopulation (0.14% of total metapopulation). Since, in principle, rather different local spatial epidemic processes can give rise to similar population level dynamics we also directly compared the spatial distribution of disease prevalence on the expected epidemic peak day t_{peak} between direct simulation and kernel corrected FSR simulation. The probability of each habitat i being infectious on day t_{peak}, p_i, was estimated using 1000 simulation replicates, and the values compared using direct and FSR simulation; the mean deviation, averaged over all habitats, between the two methods is small at just 8.5×10^{-3} (Figure 1).

In order to more efficiently assess the accuracy of the FSR simulation method under variation in parametrisation we also introduce an alternative error measure based upon the maximum difference between states in simulations using the direct and FSR methods, but using identical latent variables Z to account for stochastic fluctuations.

$$\text{Error} = \mathbb{E}_Z[\text{Error}(Z)] = \mathbb{E}_Z\Big[\sup_{t\geq 0}\Big\{\frac{1}{N}\sum_{i=1}^{N} d(X_i^{dir}(t|Z), X_i^{FSR}(t|Z))\Big\}\Big], \tag{18}$$

where $X_i^{dir}(t|Z)$ returns the disease state of the ith habitat on day t using direct simulation conditional on latent variables Z, $X_i^{FSR}(t|Z)$ is the same but where FSR simulation is used, and $d(x, y)$ is the discrete metric returning 0 iff $x = y$ and 1 otherwise. This error therefore measures the maximal difference between the spatial epidemic patterns predicted by the two methods over the entire epidemic process. This error measure has the useful property that if FSR returns identical estimates for $\{\lambda_i(t),\ t = 0, 1, \ldots, T\}_{i=1}^N$ to direct calculation then $\text{Error}(Z) = 0,\ \forall Z$. Such a relationship would not hold without matching latent variables Z, due to inherent variability between epidemic samples.

We conducted a systematic investigation of the error due to using FSR, measured using (18) and the default parameters above as a baseline comparison; averages were taken over 100 realisations of the latent variables Z. To initiate the epidemic, a single source farm was placed at the centre of the space and then surrounding farms where infected such that the initial density of infecteds $I/N = 0.02$; this allows us to match initial densities across a range of population sizes N. For the default parameters ($N = 12,100$, $L = 3$, $\Delta x = 0.5$), Error $= 6.7 \times 10^{-3}$ ($[6.2 \times 10^{-3}, 7.3 \times 10^{-3}]$ 95% confidence region). The error decayed from baseline at finer grid separation, Δx (Figure 2A). Similarly, error sharply decreased with increasing length scale of infection, L (Figure 2B). Fixing both transmission length scale (L) and grid width (Δx), and taking a sequence of epidemic models with increasing N (but keeping a constant density of habitats) we found that average error depended only weakly with N over two orders of magnitude (Figure 2C). These results are in line with both the intuition that more disperse transmission resolved on at a finer grid scale should lead to better performance, and the detailed error analysis presented in supporting information.

In addition to supremum (maximum) error over the entire epidemic, it is also of interest to assess the final error of number and spatial distribution of recovered habitats at the end of the epidemic. Again matching Z we found the final state error matched the trends observed in the supremum error, but was generally significantly lower in every part of parameter space (Figure 2). For our default scenario, the final error density was 3.84×10^{-4} ($[3.00 \times 10^{-4}, 5.84 \times 10^{-4}]$). The lower value for final error density suggests that (i) small errors in force of infection calculation due to FSR don't have a significant compound effect on the dynamic evolution of the epidemic since

the supremum error and (ii) that the large majority of errors are *timing* errors; that is errors in *when* an event occurs rather than *whether* an event occurs. Dynamically, the latent variables Z act as a set of thresholds defining when a given habitat has observed sufficient force of infection to become infected. Therefore, even small errors in the force of infection calculated using FSR have the potential to change the time-step upon which a habitat becomes infected compared to directly calculated simulation but are less likely to change whether a habitat becomes infected on any time-step. No significant systematic bias in the timing of infection was observed in the comparison of average epidemic prevalence curves generated using FSR and direct calculation, their shapes are closely similar and agree on expected peak t_{peak} (Figure 1).

The algorithmic efficiency of the FSR was measured by the time taken to simulate (serially) a number of replicate complete epidemic realisations; results are presented as an average simulation time per replicate epidemic (Figure 2D). The initial number of infected habitats was fixed to be the 2% of the total metapopulation size with the default parameterisation outlined above. For most data points 100 replicate simulations were performed for speed estimates, however, for some of the large simulations this number was reduced, but never decreased below 20. For large N there was not great variation in simulation time between individual epidemics. For FSR simulation the main determinant of speed per time step is the size of the collocation grid M, in order to compare the speed of FSR simulation to direct simulation we fixed $\Delta x = 0.5$ and $N/l^2 = 1$. As a comparison we also produced speed estimates for both discrete time simulation using direct rate calculation and for continuous time simulation based on equation (2) using the popular Gillespie algorithm [34]. For each form of simulation we found a time scaling $\mathcal{O}(N^\alpha)$ which reflects both the computational cost of force of infection recalculation and the number of time steps. Simulation time scaling was found to be approximately $\mathcal{O}(N^2)$ for both discrete time simulation using direct rate calculation ($\alpha = 1.997$) and for continuous time simulation ($\alpha = 2.121$). Simulation using FSR delivered substantial speed benefit ($\alpha = 1.503$), which can be further optimised by restricting $M = 2^n$ for $n \in \mathbb{N}$ ($\alpha = 1.390$) (Figure 2D). All simulations used for speed comparison were performed on the same 3.2 GHz desktop computer.

The maximum population size we considered for both FSR and direct simulation was $N = 105,625$ habitats, which is incidentally the same order of magnitude as the number of farms in Great Britain [35]. At this large population size the FSR method considerably outperformed the direct rate recalculation in terms of computational efficiency, running simulations in approximately 6.6% of the time. Unsurprisingly, the continuous time simulation algorithm was considerably slower than either of the other two methods. It is therefore clear that for large scale simulation of spatial epidemic outbreak together with wide sweeps of parameters space and large numbers of replicates necessary, the standard GD based simulation is only feasible when dedicated high performance computing resources are available. However, the use of discrete-time FSR simulation brings this type of calculation within the realm of powerful desktop computers.

3.1.2. FSR acceleration compared to accelerating direct simulation using pair pre-calculation

We found that for more disperse transmission kernels (larger L) the collocation grid can be coarsened (Δx can be increased) without substantially impairing accuracy and time saving is then even more dramatic. On the other hand very localised transmission demands very fine grid mesh for good accuracy, which reduces the time saving due to using FSR. So far we have compared FSR to the baseline performance of directly simulating the spatial epidemic. We now compare FSR performance against an alternative acceleration strategy based on exploiting localised transmission.

A simple acceleration technique for simulating the local spread of disease from habitat to nearby habitat is to pre-calculate effective pairs of habitats; that is those pairs of habitats where an event at one has a non-negligible effect upon the force of infection of the other. During simulation epidemic events at a habitat only cause rate updating at that habitat's effective pairs which gives an efficiency saving compared to rate updating at all remaining susceptible habitats, particularly if each habitat has only a comparatively small number of effective pairs due to localised transmission. For the Gaussian shaped kernel (17) transmission is unlikely to occur at a range greater than $5L$ and we used this range to pre-calculate effective pairs of habitats in a series of simulation speed comparisons between direct simulation and FSR simulation over a varying range of transmission

scale L ($2 \leq L \leq 17.5$) for an entire epidemic. As before habitats were uniformly randomly distributed across the box I_l at unit density ($l = 325$, $N = 105,625$) with the 2% of habitats closest to the centre of I_l chosen as the initial infectious set and other parameters as before. The size of the full set of pre-calculated habitat pairs was therefore $\mathcal{O}(NL^2)$. FSR simulation used a grid size $M = 2^m$ with m chosen as small as possible such that $L/\Delta x > 6$, a ratio of transmission range to mesh size above which FSR was found to be accurate. For larger values of L a coarser grid of fewer points could be used for FSR simulation despite a larger zero-padding domain being required to avoid periodic boundary transmission.

For the most local transmission scale considered ($L = 2$) direct simulation with pre-calculated pairs did outperform FSR (direct simulation averaged 28.50 secs per full epidemic simulation, FSR 56.45 secs per full epidemic). The computation time for pre-calculating pairs was not included in these averages. However, on the desktop used epidemic simulation time increased rapidly with L for the pair pre-calculation method despite epidemics with small L typically requiring more time steps to simulate until the end. By contrast FSR simulation became faster for increasing L reflecting a typically shorter epidemic and sharply faster whenever a coarser grid could be used (Figure 3). The cross-over point was at $L \approx 3$, by $L = 5$ FSR was significantly more efficient at simulating full epidemics compared to direct simulation with pre-calculated pairs (direct simulation averaged 48 secs per full epidemic simulation, FSR 8.5 secs per full epidemic).

Certainly there exists the potential to further optimise direct simulation through more efficient pair searching and using systems with greater available RAM. There also exist other methods of accelerating direct simulation such as the subdivision of I_l into cells and exploiting the property that transmission to distant cells is highly unlikely, an example of such a method is given by Keeling and Rohani [33]. However, pair pre-calculation is representative of acceleration techniques for spatial epidemics extant in the literature in that performance improves as transmission becomes more local. In general these acceleration methods are less successful whenever each habitat has a large number of effective pairs, whether this is due to long range transmission, heavy-tailed transmission or spatial clustering of the metapopulation. FSR is effective in accelerating simulation

for longer range transmission irrespective of metapopulation density, and therefore is a successful strategy in a different problem domain from typical acceleration techniques. Heuristically, for very localised transmission, the force of infection for a susceptible habitat can be compactly represented as a truncated sum over only a comparatively small number of nearby infectious habitats but would require many discrete modes for description in the spatial frequency domain used for FSR convolution solving. The converse is that for disperse transmission a significant fraction of the total population of infectious habitats contribute to the infection hazard for each susceptible habitat, whereas in the frequency domain only a comparatively small number of modes are required for a good description of the force of infection field.

3.2. Accelerated Likelihood Calculation

Likelihood based inference plays an important role in parameter estimation, and hence is key to matching models with observations. From a classical statistics point of view the maximum likelihood estimator (MLE), that is the parameter values which maximise the likelihood of the observations, is viewed as the set of parameters that best captures the dynamics (see Casella and Berger [36] for an introduction to classical likelihood methods). Additionally, for parameter inference by Markov Chain Monte Carlo (MCMC) [37, 38, 39] the calculation of likelihood ratios is a necessary, and often computationally intensive step. Hence the improvement in speed offered by the FSR method has clear advantages in parameter inference if the results are sufficiently accurate.

As an example of the computational efficiency gains for data imputation derived from using the FSR algorithm we present a simulated outbreak amongst $19,600$ habitats generated using the simplified model given above. The random habitat locations are given within I_l with $l = 140$ as the points of a Poisson cluster process [40] chosen so as to give positive spatial correlation between locations. The transmission kernel was chosen as heavy-tailed,

$$K(|x|) = \frac{\beta}{(2\pi(1+|x|^2))^{3/2}}, \qquad K \sim |x|^{-3}. \tag{19}$$

Magnitude$(K) = \beta$ represents the infectiousness of the disease. The target for imputation is the infectious intensity β, using the retrospective infection events up until $t = 30$ days. We treat the

removal rate (chosen so that average period of infectiousness was 4 days) and the shape of the transmission kernel as known data. In keeping with our final example on livestock epidemics, the parameters chosen here roughly correspond to those for the 2001 UK Foot-and-Mouth outbreak [18].

For a given epidemic realisation we denote the set of populations that are first infected on day t, $\mathcal{I}(t)$, and the set of populations that are susceptible at the beginning of day t and avoid infection on that day, $\mathcal{S}(t)$. The likelihood $\mathcal{L}$ of the observed sequence of infections for a given transmission rate β is given in terms of the per day transmission probabilities [41],

$$\mathcal{L}(\beta|\{\mathcal{I}(t),\mathcal{S}(t)\}_{t=0}^{T}) = \mathbb{P}(\{\mathcal{I}(t),\mathcal{S}(t)\}_{t=0}^{T}|\beta) = \prod_{t=0}^{T}\Big[\prod_{i\in\mathcal{I}(t)}\left(1-e^{-\lambda_i(t)}\right)\prod_{j\in\mathcal{S}(t)}e^{-\lambda_j(t)}\Big]. \tag{20}$$

The likelihood of a full data set $\mathcal{D}$, including removals and any other stochastic events, can then be derived similarly by augmenting with their per day probabilities. We note that calculating the likelihood (20) involves the sequential recalculation of the daily rates of infection $\lambda_i(t)$ for each susceptible population i. This is exactly the task the FSR algorithm has been designed to achieve with great numerical efficiency.

For a randomly chosen initially infected habitat (individual) with infectious intensity $\beta_{true} = 0.75$ a sample of an invasive epidemic was generated (Figure 4). This outbreak was characterised by long range invasion of clusters of higher local density of habitats followed by intense spreading within the cluster. The available data was assumed to be the set of infection and recovery events for the first 30 time-steps (days) of the outbreak. The log-likelihood profile $\log\mathcal{L}_{profile}(\beta)$ for the interval $\beta \in [0.1, 2.1]$ at a resolution of $\Delta\beta = 0.01$ was calculated from (20) using both direct recalculation and kernel corrected FSR for the daily infection rates (the approximating grid width used for FSR was $\Delta x = 0.5$). The constructed log likelihood values were numerically close especially around the peak, such that not only were the two implied maximum likelihood estimators indistinguishable $\hat{\beta}_{dir} = \hat{\beta}_{FSR} = \beta_{true} = 0.75$, but also the 99.9% confidence intervals $\beta \in [0.71, 0.79]$ were also in exact numerical agreement (Figure 4).

Constructing the full log likelihood profile using the FSR rate calculation took 16.5% of the time required to construct the log likelihood profile using direct rate calculation. Such a time saving was consistent with the accelerated simulation performance found in the previous section (Figure 2D). The imputation method used in this section was accelerated by using FSR rate recalculation only because each likelihood calculation (20) was accelerated. This suggests that any statistical method for the class of spatial epidemic models considered in this work which require repeated likelihood, or likelihood ratio, calculations could be accelerated by using FSR.

3.3. Case Study: Forecasting Epidemic Outbreak Amongst US Cattle Farms

In this final section we apply the FSR methodology to determine the impact of an epidemic spreading amongst US cattle farms and to investigate how this depends upon transmission assumptions, such as the decay tail of the transmission kernel and the infectious intensity of the disease. We performed repeated simulations to determine the distribution of epidemic severity using a modified version of the spatial force of infection (1) that takes into account the numbers of cattle at both infectious and at-risk susceptible farms. Data for US farm locations and their cattle holding sizes is only available aggregated at the county-scale. We circumvented this missing information by generating a synthetic data set of randomised farm locations (with each county) and their cattle numbers which is consistent with aggregate US agricultural census data at the county level. It is this synthetic data set of $93,777,559$ cattle distributed across $1,018,877$ farms that we used to generate epidemic realisations. The continent-wide nature of the epidemic and the necessity of performing multiple simulations per parameter choice represented a major computational challenge. The FSR simulation method presented in this work accelerated simulation sufficiently as to make predictive Monte Carlo modelling for a range of parameter choices feasible using a standard desktop computer; without an accelerated simulation method this investigation would be impracticable without far greater computational resource.

3.3.1. Farm Infection Model and FSR Simulation with Demography

The livestock disease being modelled was considered to be sufficiently infectious that once introduced into a naive farm it spread rapidly amongst all the livestock present. This motivates the decision to represent the epidemic state of the *farm* by a single infection state. The within farm

disease progression was represented by two stages, as in Keeling et al. [18] for Foot-and-Mouth Disease (FMD); an initial exposed (E) period of 4 days during which the infected farm does not actively recruit to the epidemic and a subsequent actively infectious (I) period of 5 days before detection and removal. We do not include additional veterinarian tracing efforts such as identifying dangerous contacts (DC) of detected infectious farms, or any form of additional control based on geographic proximity to the detected infectious farm (such as contiguous premise (CP) or ring culling). Therefore, this model reflects a control effort directed only at removing detected infected premises (IP) which is the simplest and least disruptive of possible control policies.

We follow Tildesley et al. [24, 42] in extending the basic spatial force of infection (1) to include a non-linear dependency on the number of cattle (N_i) in both susceptible and infectious farms,

$$\lambda_i(t) = N_i^p \sum_{j=1}^{N} K(x_i - x_j) N_j^q I_j(t). \tag{21}$$

The power parameters p, q scale, respectively, the dependence of farm susceptibility and transmissibility upon cattle numbers. For the 2001 FMD outbreak the power parameters for cattle numbers have been found to vary regionally between 0.2 and 0.44 [24]. We chose $p = q = 0.2$ for all US regions which corresponds to the minimal amount of demographic dependence within the inferred range ($p = q = 0$ recovers the demography-free model (1)). The FSR collocation grid approximated a projection of the USA onto a plane with additional zero-padding extending 500 km from the southern most and eastern most tips of contiguous USA. We chose the FSR collocation grid size so that M was product of powers of 2 and 3 for numerical efficiency. The grid width was 3.6 km north/south and 4.6 km west/east, which were a finer scale than the length scales of transmissions considered below. Gaussian approximations were used with $\epsilon = 4$ km. Simulating epidemic realisations with the daily risk model (21) required a small modification to the FSR method. When updating blurry image of infection f_I^ϵ at local points to farm j a factor N_j^q is used to increase the mass of the Gaussian approximation of farm j. The approximate force of infection used for FSR

simulation with demography is,

$$\lambda_i(t) \approx N_i^p \lambda_{PS}^{M,\epsilon}(x_i, t). \tag{22}$$

The pseudo-spectral approximation for point x_i being given by bi-linear interpolation from its 4 nearest collocation grid points. All statistics in this section were estimated from 1000 independent FSR simulations of a complete epidemic.

We are interested in the impact on epidemic severity of the decay tail of the transmission kernel, and moreover how this tail affects the upper quantiles for outbreaks severity, quantities of considerable public policy importance. To achieve this we simulate outbreaks using a family of kernels $K_a(|x|) \sim |x|^{-a}$,

$$K_a(|x|; L) = \beta \mathcal{N}_a(L)(L^2 + |x|^2)^{-a/2}, \qquad a = 3, 4, 5, \tag{23}$$

where β is the transmissibility of the disease, $\mathcal{N}$ normalises the transmission kernel so that Magnitude$(K) = \beta$ and L is a length scale parameter. Each transmission kernel is heavy-tailed in the sense of Kot et al due to each kernel having infinite moments of dispersal distance [20]. Nevertheless, K_3 and K_5 represent rather different transmission tail behaviour within the general family of heavy-tailed kernels; a consequence of the heavy-tailed decay of K_3 is that both mean and variance of the dispersal distance (as given by (14) and (16)) are infinite for all $L > 0$ whereas both these dispersal range measures are finite for K_5. Transmission kernel K_4 gave an intermediate class of transmission tail behaviour; Mean$(K_4) = (\pi/2)L$ is finite whereas Var$(K_4) = \infty$ for $L > 0$. In the subsequent simulation study we choose L so that Mean(K_5) = Mean(K_4) = 20 km. The heavy tailed kernel K_3 cannot be matched in this manner: $L = 10$ km was chosen as its length scale.

3.3.2. Transmission Tail Decay and Variable Severity

Each epidemic realisation was initiated by a single infectious farm located in Franklin County, Texas. This choice of initial location can be considered pessimistic from the point of view of disease control due to its proximity to cattle farm high density regions in Texas and the central plains.

Despite the favourable initial location for the disease the range of epidemic sizes were found to be multi-modal. For all transmission kernels, and even for the greatest infectious intensity considered ($\beta = 0.115$), there was a significant probability of only a small epidemic occurring (P_{small}), defined as at most 50 farms becoming infected. For the finite mean dispersal kernels, with $\beta = 0.115$, the probability of a small epidemic probability was similar ($P_{small}(K_4) = 0.428$ and $P_{small}(K_5) = 0.434$); whereas for the heavy tailed kernel K_3 the probability of a small epidemic occurring was greater ($P_{small}(K_3) = 0.537$).

The most severe epidemic predicted led to almost $140,000$ infected cattle farms (13.7% of US total). For the finite kernels (K_4 and K_5) those epidemics which do take hold and produce a nation-wide epidemic were found to be multi-modal in their distribution of final number of disease affected farms (Figure 5) with both large and intermediate scale epidemics common. The number of farms affected during a given epidemic realisation reflected that epidemic's success in invading different high-risk regions; in order of most to least likely of having a large-scale outbreak these high-risk regions are: Texas, the central plains, the Ohio river basin and South-Eastern Pennsylvania (Figure 6). Given this multi-modal behaviour for epidemic sizes it is more natural to focus on quantiles of outbreak size as a representative statistics for severity. However, epidemics with a heavy tailed transmission kernel, K_3, displayed rather different behaviour. Epidemic severity with heavy tailed transmission became strongly bi-modal as the infectious intensity β was increased; the epidemics forecast were either small or tightly clustered around a large epidemic size (Figure 5).

As well as simply examining the number of farms infected, the spatial distribution of these farms is of important applied interest as it relates to the necessary distribution of control resources. In all our simulations, the western half of USA largely escaped infection for finite mean kernels. The infinite dispersal variance kernel K_4 had consistently more severe 75% and 97.5% quantiles of outbreak size compared to K_5, and we think of these upper quantiles as reasonable worst-case scenarios. This reflects that a long-range dispersal event from one farm cluster to a distant one was more likely for this kernel despite matched mean dispersal range and equal total transmission rates; the slower spatial decay of the K_4 kernel was a significant factor in determining the range of

plausible worst-case scenarios for US cattle epidemic forecasting (Figure 6). Risk of infection for epidemics with heavy tailed transmission kernel K_3 was more evenly distributed in space than for the finite mean kernels K_4 and K_5. Nonetheless, there are regions in Texas, the central plains, the Ohio river basin and South-Eastern Pennsylvania where greater risk of infection was observed for all three kernels, although naturally K_3 and K_4 shows the greatest spread from the initial source in Texas.

If we are considering an outbreak of Foot-and-Mouth in the USA, then there is uncertainty in the transmission constant β as well as the shape of the transmission kernel. For a less infectious disease ($\beta \leq 0.095$) the 75% quantiles of outbreak size was significantly smaller for the K_3 model than for the K_4 or K_5 models. This is because the outbreak is initialised in a region of high cattle and farm density; therefore more dispersed kernels simply waste infection by placing more transmission away from this high-density region. Therefore this most dispersed kernel leads to the greatest risk of early extinction. By contrast for more infectious diseases ($0.095 < \beta < 0.115$) the 75% quantiles for epidemics with transmission kernel K_3 was significantly greater than for the more localised transmission kernels. The upper extreme 97.5% quantiles for epidemic outcomes with either K_3 or K_4 transmission kernel were similar; the 'worst case' scenarios for either transmission models were similar in that either model could predict invasion into a number of important areas for US cattle farming and further afield. For the most infectious disease intensities considered ($\beta \geq 0.11$) the local transmission kernel K_5 also predicted similar 97.5% quantiles (Figure 6).

The predicted spatial patterns of disease incidence and multi-modal severity have important implications for emergency disease control in response to an epidemic outbreak amongst US cattle farms. The proportion of outbreaks predicted to cause national-scale epidemics suggests that control efforts based only on removal of IPs, as simulated here, may be insufficient to control disease spread amongst US cattle farms. This result is in line with findings for the 2001 UK foot-and-mouth outbreak [18, 43]. The areas at most risk and the overall severity of a predicted outbreak were found to depend crucially on the tail of the transmission kernel. For transmission kernels K_4 and K_5 incidence was found to vary strongly across the country reflecting both the density of farms

and livestock and the ease with which infection can reach an area. This suggests that a regional (state or county) level control method, such as local movement bans, might be effective at reducing epidemic burden. In contrast, epidemics predicted using a very heavy tailed transmission (K_3), showed far more limited spatial heterogeneity which combined with the heavier tail suggests that regionally based control would be unlikely to be successful. This echoes findings for the heavy-tailed dispersal of sudden oak death in California [44] albeit at a greater spatial scale. Moreover, the qualitative distinction between predicted epidemic outcomes with K_3 kernel and K_4/K_5 kernels cannot be explained in analogy to analytic results for simpler models [21, 20, 22] since each kernel falls into the general 'heavy-tailed' phenomenological category. This detailed sensitivity of outcome upon the tail of the transmission kernel emphasises the need for numerically efficient methods for forecasting simulations in order to best inform response to epidemic outbreak. The FSR simulation method is designed to both accelerate the generation of epidemic forecasts and inference techniques that require repeated calculation of likelihoods.

4. Discussion

We have considered the stochastic simulation of a very common class of models for the spatial dispersion of an invasive infection. In particular, we have demonstrated a novel method for recalculating the stochastic transition rate using a convolution solution that can deliver significant time saving to large scale Monte Carlo investigations. The convolution solution uses only 'out-of-the-box' software for implementation that is readily and freely accessible, moreover the analytic properties of the error in spectral convolution solving are well understood.

Since the FSR method is an addendum to commonly used stochastic simulation algorithms it is flexible and is not restricted to solely SIR type spatial epidemic modelling. Rather, the FSR method is a possible tool for accelerating simulation of models concerned with spatial dispersal where the dispersion kernel is translation invariant and smooth. It should be noted that the treatment of habitats as point locations is a simplifying modelling assumption in order to allow the force of infection to be written as a weighted sum over infected habitats. The FSR method allows the very natural relaxation of this assumption to modelling scenarios where habitats have spatial extent. In

addition, the assumption used throughout that each habitat equates to a single host is also trivially relaxed.

The need for rapid spatial transmission rate calculations is not just restricted to investigating simulated outcomes of stochastic models; it also plays a vital role in parameter estimation and inference. We have shown that FSR can substantially accelerate the calculation of a full log-likelihood profile for a parameter when the likelihood function can calculated from available data. Likelihood calculation is also a necessary but computationally intensive step in a number of variants of MCMC inference; these typically involve sequential calculations of transition rates between events in order to define an acceptance probability for a proposed set of parameters. MCMC inference is often preferred when the data required to calculate the likelihood function is only partially observed, a standard strategy being to augment missing data as additional parameters to be imputed. Data augmented MCMC has been applied to epidemic inference with both non-spatial transmission [45] and spatial transmission models [39]. FSR can accelerate the calculation of acceptance probabilities for data augmented MCMC inference for the spatial models considered in this work. An intriguing alternative approach to bayesian parameter estimation of partially observed spatial epidemics could be to use FSR simulation in combination with an approximate bayesian computation (ABC) imputation method. ABC methods rely intensively upon recursive simulation using parameter sets drawn from their prior joint distribution and have become very popular in parameterising theoretical biological models [26, 27] including epidemic models [25]. The computational overhead of ABC methods is nearly entirely due to the necessary generation of a very large number of simulated epidemic outcomes for comparison to data. FSR could substantially improve the performance of ABC methods for spatial models simply by decreasing the average time taken per epidemic simulation.

When dispersion is highly localised a different method for accelerating rate recalculation should be considered. There are a number of efficient simulation strategies for localised transmission epidemics extant in the literature and we consider pair pre-calculation as an example of these. The strength of the FSR method is that it is effective at accelerating spatial simulations in the alternative scenario of heavy-tailed dispersion where there are fewer well known methods for accelerating

performance of explicitly spatial simulations. Ultimately the best simulation method will be problem specific, FSR is intended as a tool for accelerating spatially explicit epidemic simulations with heavy-tailed transmission.

FSR is also successful for large metapopulation simulations, whether that refers to the existence of many habitat locations or large local populations at each habitat, with long-range dispersion. Using the FSR simulation method we were able to make continent-wide epidemic predictions for disease spread amongst US cattle farms; modelled at the scale of the individual farm unit. The highly stochastic nature of epidemic outcomes required many MC replicate simulations for the good statistical confidence of each transmission scenario considered. Our simulation study suggested that areas of USA are at considerable risk of large numbers of cattle infections in the event of epidemic outbreak. In particular the sensitivity of US farm epidemic outcomes to the tail-decay of the transmission kernel further emphasises the need to robust and large scale predictive modelling for both scenario forecasting and statistical inference. The considerable efficiency of the FSR method promises to facilitate such a large-scale, and detailed, epidemic modelling.

Acknowledgments

We thank L. Danon (University of Warwick) for fruitful discussion on the presentation of our results, T. House (University of Warwick) for useful comments on comparing stochastic epidemics and V. Jansen (Royal Holloway, University of London) for suggesting kernel correction to improve accuracy. The lead author acknowledges EPSRC funding for this work. This work is supported by the RAPIDD program of the Science and Technology Directorate, Department of Homeland Security, and the Fogarty International Center, National Institutes of Health and the Foreign Animal Disease Modelling program of the Science and Technology Directorate, Department of Homeland Security contract HSHQDC-13-C-B00028.

[1] R. M. Anderson, R. M. May, Infectious diseases of humans., Oxford University Press, New York, 1992.

[2] D. Smith, B. Lucey, L. Waller, J. Childs, L. Real, Predicting the spatial dynamics of rabies

epidemics on heterogeneous landscapes, Proceedings of the National Academy of Sciences of the United States of America 99 (6) (2002) 3668–3672.

[3] M. Keeling, M. Woolhouse, R. May, G. Davies, B. Grenfell, Modelling vaccination strategies against foot-and-mouth disease, Nature 421 (6919) (2003) 136–142.

[4] M. J. Tildesley, N. J. Savill, D. J. Shaw, R. Deardon, S. P. Brooks, M. E. J. Woolhouse, B. T. Grenfell, M. J. Keeling, Optimal reactive vaccination strategies for a foot-and-mouth outbreak in the UK, Nature 440 (7080) (2006) 83–86.

[5] J. Murray, E. Stanley, D. Brown, On the spatial spread of rabies among foxes, Proceedings of the Royal society of London. Series B. Biological sciences 229 (1255) (1986) 111–150.

[6] C. Barrett, K. Bisset, S. Eubank, X. Feng, M. Marathe, Episimdemics: an efficient algorithm for simulating the spread of infectious disease over large realistic social networks, Proceedings of the 2008 ACM/IEEE conference on Supercomputing (2008) 1–12.

[7] M. J. Keeling, K. T. D. Eames, Networks and epidemic models, Journal of the Royal Society Interface 2 (2005) 295–307.

[8] R. Levins, Some Demographic and Genetic Consequences of Environmental Heterogeneity for Biological Control, Bull. Entomol. Soc. Am. 15 (1969) 237–240.

[9] I. A. Hanski, M. E. Gilpin (Eds.), Metapopulation Biology: Ecology, Genetics, and Evolution, 1st Edition, Academic Press, New York, 1997.

[10] I. Hanski, O. Gaggiotti, Ecology, evolution and genetics of metapopulations, Academic Press, New York (2004).

[11] O. Ovaskainen, S. Cornell, Space and stochasticity in population dynamics, Proceedings of the National Academy of Sciences 103 (34) (2006) 12781–12786.

[12] S. Cornell, O. Ovaskainen, Exact asymptotic analysis for metapopulation dynamics on correlated dynamic landscapes, Theoretical Population Biology 74 (2008) 209–225.

[13] I. Hanski, A practical model of metapopulation dynamics, Journal of Animal Ecology 63 (1) (1994) 151–162.

[14] M. Heino, I. Hanski, Evolution of Migration Rate in a Spatially Realistic Metapopulation Model, The American Naturalist 157 (5) (2001) 495–511.

[15] G. J. Gibson, Investigating Mechanisms of Spatiotemporal Epidemic Spread Using Stochastic Models, Phytopathology 87 (2) (1997) 139–146.

[16] A. L. Lloyd, V. A. A. Jansen, Spatiotemporal dynamics of epidemics: synchrony in metapopulation models, Mathematical Biosciences 188 (1-2) (2004) 1–16.

[17] B. Grenfell, B. Bolker, A. Kleczkowski, Seasonality and extinction in chaotic metapopulations, Proceedings of the Royal society of London. Series B. Biological sciences 259 (1995) 97–103.

[18] M. J. Keeling, M. E. Woolhouse, D. J. Shaw, L. Matthews, M. Chase-Topping, D. T. Haydon, S. J. Cornell, J. Kappey, J. Wilesmith, B. T. Grenfell, Dynamics of the 2001 UK foot and mouth epidemic: stochastic dispersal in a heterogeneous landscape, Science (New York, NY) 294 (5543) (2001) 813–817.

[19] N. M. Ferguson, C. A. Donnelly, R. M. Anderson, The Foot-and-Mouth Epidemic in Great Britain: Pattern of Spread and Impact of Interventions, Science 292 (5519) (2001) 1155–1160.

[20] M. Kot, M. A. Lewis, P. van den Driessche, Dispersal data and the spread of invading organisms, Ecology 77 (7) (1996) 2027–2042.

[21] D. Mollison, Dependence of epidemic and population velocities on basic parameters, Mathematical Biosciences 107 (2) (1991) 255–287.

[22] M. Lewis, S. Pacala, Modeling and analysis of stochastic invasion processes, Journal of Mathematical Biology 41 (5) (2000) 387–429.

[23] M. W. Shaw, Simulation of Population Expansion and Spatial Pattern when Individual Dispersal Distributions do not Decline Exponentially with Distance, Proceedings of the Royal Society B: Biological Sciences 259 (1356) (1995) 243–248.

[24] M. Tildesley, R. Deardon, N. Savill, P. Bessell, S. Brooks, M. Woolhouse, B. Grenfell, M. Keeling, Accuracy of models for the 2001 foot-and-mouth epidemic, Proceedings of the Royal Society B: Biological Sciences 275 (1641) (2008) 1459–1468.

[25] T. McKinley, A. R. Cook, R. Deardon, Inference in Epidemic Models without Likelihoods, The International Journal of Biostatistics 5 (24) (2009) 1–37.

[26] K. Csillery, M. G. B. Blum, O. E. Gaggiotti, O. Francois, Approximate Bayesian Computation (ABC) in practice, Trends in Ecology & Evolution 25 (7) (2010) 1–9.

[27] M. A. Beaumont, Approximate Bayesian Computation in Evolution and Ecology, Annual Review of Ecology, Evolution, and Systematics 41 (1) (2010) 379–406.

[28] D. Gillespie, Approximate accelerated stochastic simulation of chemically reacting systems, The Journal of Chemical Physics 115 (2001) 1716–1733.

[29] J. Hesthaven, S. Gottlieb, D. Gottlieb, Spectral methods for time-dependent problems, Cambridge University Press, Cambridge (2007).

[30] T. Sellke, On the asymptotic distribution of the size of a stochastic epidemic, Journal of Applied Probability 20 (1983) 390–394.

[31] A. Cook, G. Gibson, T. Gottwald, C. Gilligan, Constructing the effect of alternative intervention strategies on historic epidemics, Journal of the Royal Society Interface 5 (27) (2008) 1203–1213.

[32] G. Friedlander, M. Joshi, Introduction to the Theory of Distributions, 2nd Edition, Cambridge University Press, Cambridge, 1998.

[33] M. J. Keeling, P. Rohani, Modeling Infectious Diseases in Humans and Animals, Princeton University Press, 2008.

[34] D. T. Gillespie, Exact stochastic simulation of coupled chemical reactions, The Journal of Physical Chemistry 81 (25) (1977) 2340–2361.

[35] I. Chis Ster, N. Ferguson, Transmission parameters of the 2001 foot and mouth epidemic in Great Britain, PLoS One 2 (6) (2007) e502.

[36] G. Casella, R. L. Berger, Statistical Inference, 2nd Edition, Duxbury, Pacific Grove, 2010.

[37] W. R. Gilks, S. Richardson, D. J. Spiegelhalter (Eds.), Markov Chain Monte Carlo in Practice, Chapman & Hall, London, 1996.

[38] P. D. P. O'Neill, A tutorial introduction to Bayesian inference for stochastic epidemic models using Markov chain Monte Carlo methods., Mathematical Biosciences 180 (2002) 103–114.

[39] G. J. Gibson, W. Otten, J. A. N Filipe, A. Cook, G. Marion, C. A. Gilligan, Bayesian estimation for percolation models of disease spread in plant populations, Statistics and Computing 16 (4) (2006) 391–402.

[40] P. Diggle, Statistical analysis of spatial point patterns, Academic Press, London, 1983.

[41] R. Deardon, S. Brooks, B. Grenfell, M. Keeling, M. Tildesley, N. Savill, D. Shaw, M. Woolhouse, Inference for individual-level models of infectious diseases in large populations, Statistica Sinica 20 (1) (2010) 239–261.

[42] M. Tildesley, T. House, M. Bruhn, R. J. Curry, M. O'Neil, J. L. E. Allpress, G. Smith, M. J. Keeling, Impact of spatial clustering on disease transmission and optimal control, Proceedings of the National Academy of Sciences 107 (3) (2010) 1041–1046.

[43] N. M. Ferguson, C. A. Donnelly, R. M. Anderson, Transmission intensity and impact of control policies on the foot and mouth epidemic in Great Britain, Nature 413 (6855) (2001) 542–548.

[44] J. A. N. Filipe, R. C. Cobb, R. K. Meentemeyer, C. A. Lee, Y. S. Valachovic, A. R. Cook, D. M. Rizzo, C. A. Gilligan, Landscape epidemiology and control of pathogens with cryptic and long-distance dispersal: sudden oak death in northern Californian forests., PLoS Computational Biology 8 (1) (2012) e1002328.

[45] P. D. O'Neill, G. O. Roberts, Bayesian Inference for Partially Observed Stochastic Epidemics, Journal of the Royal Statistical Society A (1999).

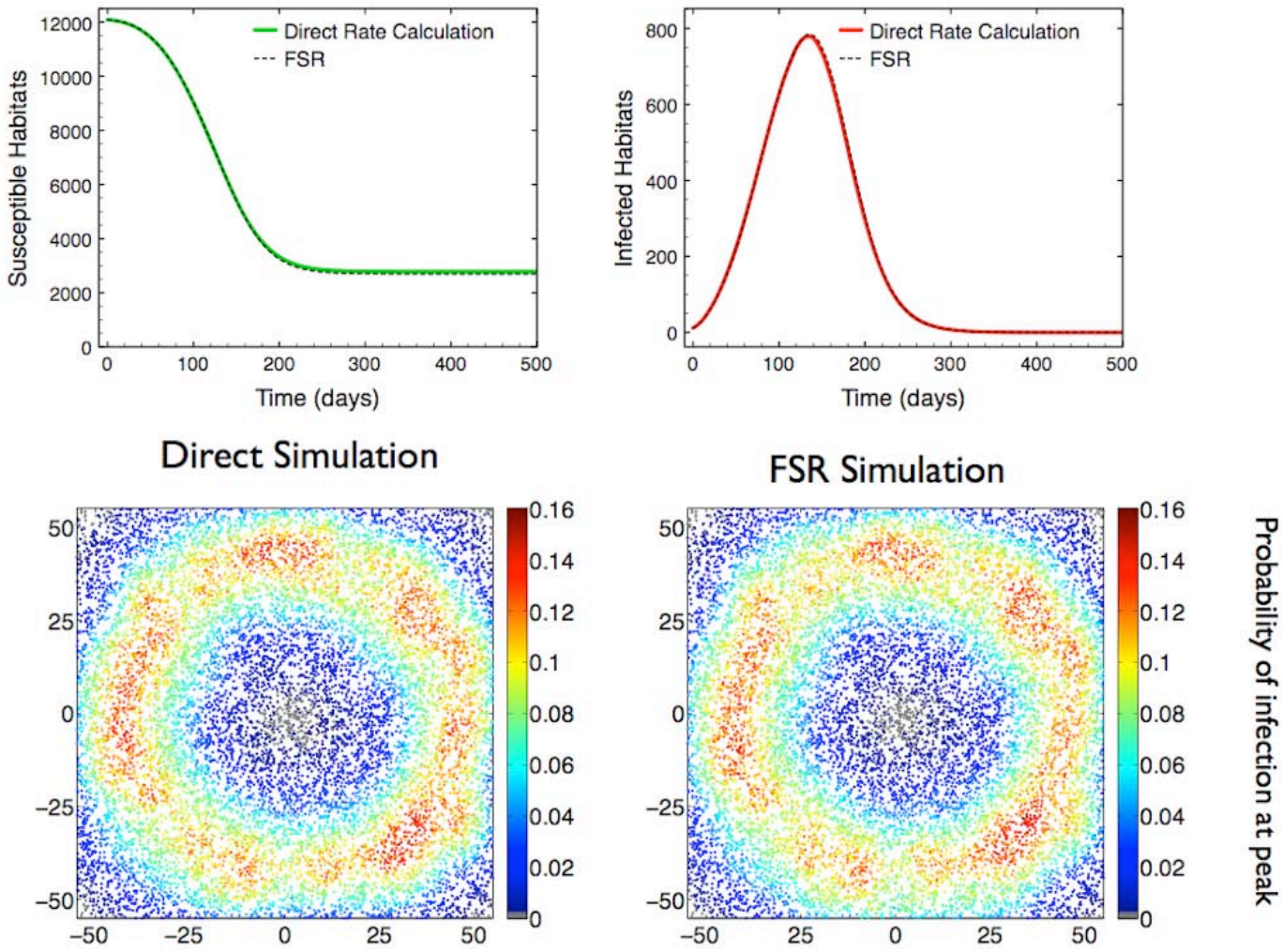

Figure 1: A comparison between the epidemic spatio-temporal distributions resultant from direct simulation and fast spectral (FSR) simulation. $N = 12\,100$ habitats were distributed uniformly at random over a 110×110 box. Initial seed was chosen at random and shifted to origin, with 9 closest farms also infected at $t = 0$. Spatial transmission parameters were $L = 3$, $\beta = 0.2$. The FSR parameters were $\Delta x = 0.5$ and $\epsilon = 0.4$. *Top Row:* Expected dynamics of number of susceptible (left) and infected (right) habitats estimated from 1000 simulation replicates, 6σ deviation was found to be tight on curves and is not shown. Coloured lines give the dynamics calculated using direct summation of rates, black lines give the FSR results. The worst inaccuracy on any day in expected number of infecteds for FSR simulation was 16.85 habitats (0.14% of metapopulation). *Bottom Row:* Spatial probability of being infectious at epidemic peak ($t_{peak} = 134$ days), estimated from 1000 simulation iterates, for direct simulation (left) and FSR simulation (right). The FSR method captures the spatial distribution of epidemic risk; the mean absolute deviation in infected probability at peak was 8.5×10^{-3}.

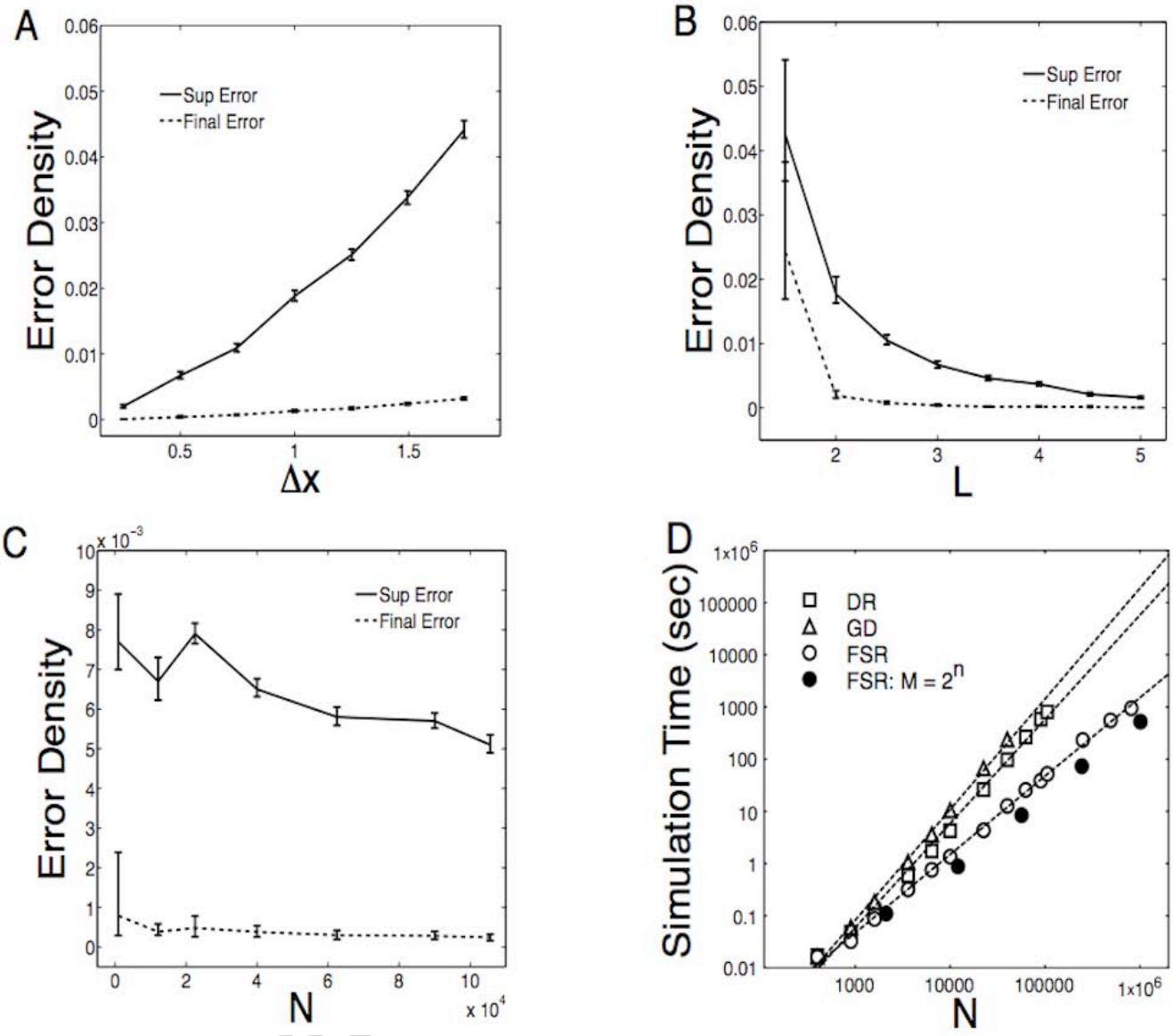

Figure 2: A Comparison between direct simulation and FSR simulation for epidemic spread amongst an explicitly spatial Levins-type metapopulation. Latent variables were matched in order to directly compare simulation methods, and comparisons taken over 100 matched MC replicates. All confidence intervals are due to bias corrected 95% confidence boot-strapping. The base set of parameter was $N = 12\,100$, $\Delta x = 0.5$, $L = 3$, $\beta = 0.2$, $\gamma = 0.1$ with a Gaussian-shaped transmission kernel. **A-C**: Varying the base parameter set in, respectively, Δx, L, and N. As expected from theoretical considerations, the density of errors between direct simulation and FSR simulation is increasing with Δx, decreasing with L and only weakly dependent on N. **D**: Time taken per replicate simulation for the base set of parameters as N varies fitted to the power-law scaling N^{α}. The size of the FSR collocation grid M is chosen so that $\Delta x = 0.5$ is fixed with a unity density of habitats. For small value of N there is very little gain in using FSR, but as N increases the time saving becomes increasingly favourable. Daily time step simulation with direct rate recalculation (squares; DR) appeared to scale as approximately $\mathcal{O}(N^2)$ (log-log slope of 1.997). As a comparison continuous time simulation using the Gillespie Direct algorithm was also considered (triangles; GD) and also found to scale as approximately $\mathcal{O}(N^2)$ (log-log slope of $\alpha = 2.121$). The computational cost for the FSR method (circles; FSR) was fitted by a log-log slope of $\alpha = 1.503$ (black dashed line) which indicated substantially reduced time per simulation due to using FSR as N becomes large. The speed performance of FSR was optimised by choosing M as an integer power of 2 (filled circles), which fits to a slope $\alpha = 1.390$ (slope not shown).

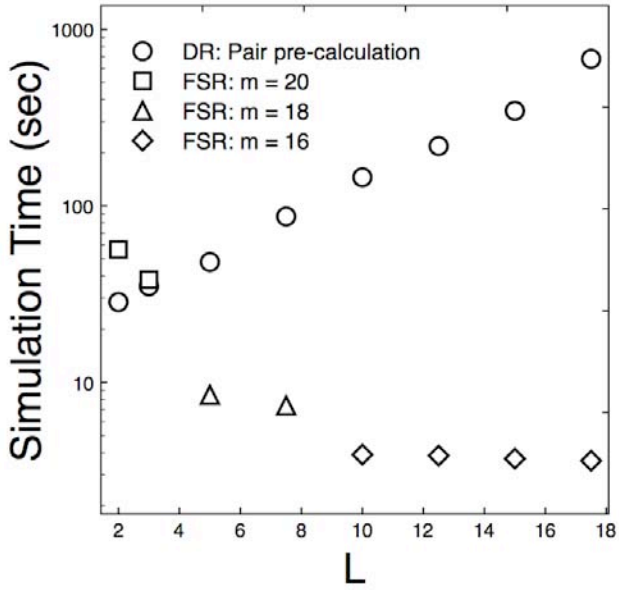

Figure 3: Mean time taken per replicate simulation for a large simulation ($N = 105,625$) with base set of parameters $\beta = 0.2$, $\gamma = 0.1$ with a Gaussian-shaped transmission kernel. The efficiency of direct simulation with pair pre-calculation (circles) is compared to FSR simulation (squares, triangles and diamonds) for a varying range of typical transmission scale L. The FSR grid size $M = 2^m$ was chosen as small as possible whilst respecting a transmission scale to grid width ratio for which FSR is accurate ($L/\Delta x > 6$). For local transmission ($L = 2$) pre-calculating pairs is a more efficient strategy than FSR. However, FSR becomes sharply more efficient as L increases due to using a smaller solution grid and the epidemic being typically shorter in duration. Pair pre-calculation becomes rapidly less efficient as L increases due to the set of effective pairs being held in memory becoming excessively large.

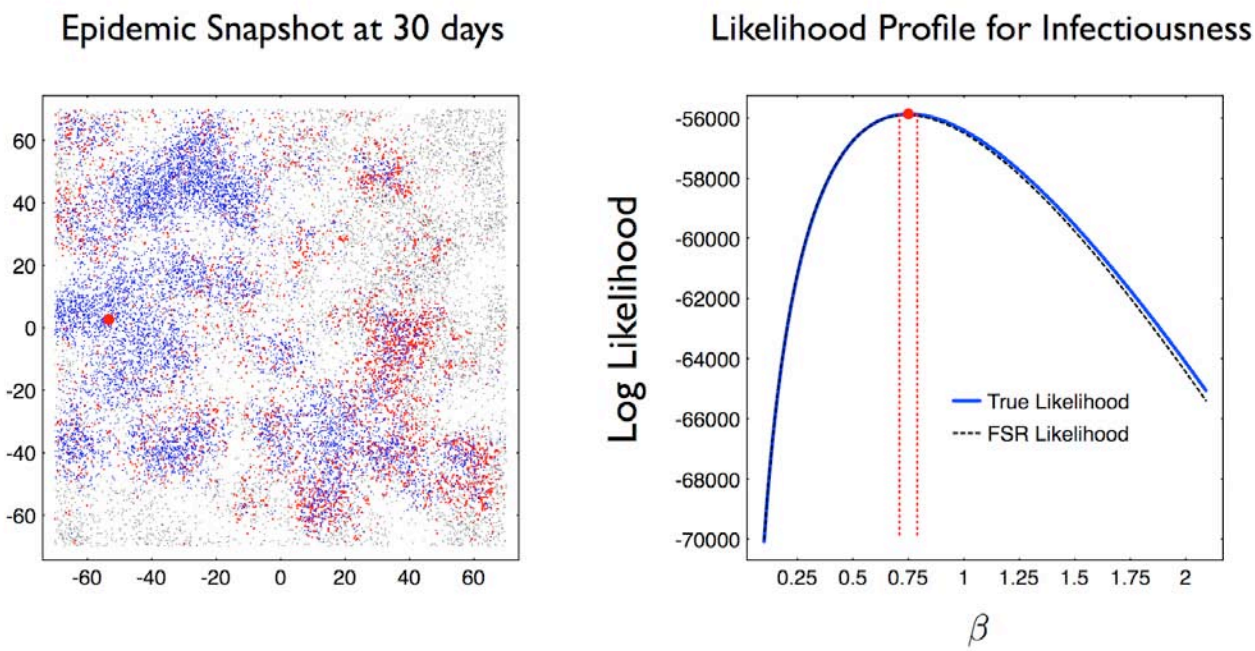

$$\log \mathcal{L}(\beta) = \sum_{t=0}^{T} \Big[\sum_{i \in \mathcal{I}(t)} \log \left(1 - e^{-\lambda_i(t)}\right) - \sum_{j \in \mathcal{S}(t)} \lambda_j(t) \Big]$$

Figure 4: Maximum likelihood inference for a spatial metapopulation epidemic model. A single epidemic realisation was generated using heavy tailed transmission kernel (19) with infectious intensity $\beta = 0.75$. *Left*: A snapshot of the epidemic progression after 30 days. Each point represents the location of a susceptible (grey), infected (red) or removed (blue) habitat. The large red point denotes the location of the initial infected habitat. The available data for imputation were the daily infection and recovery events up to this day. *Right:* Log likelihood profiles for the data under variation of β calculated directly and using the FSR rate approximation. Both profiles imply an identical maximum likelihood estimator $\hat{\beta} = 0.75$ and identical 99.9% confidence intervals $\beta \in [0.71, 0.79]$. The FSR method took 16.5% of the time to construct the full likelihood profile; this was consistent with the acceleration found when comparing simulation methods.

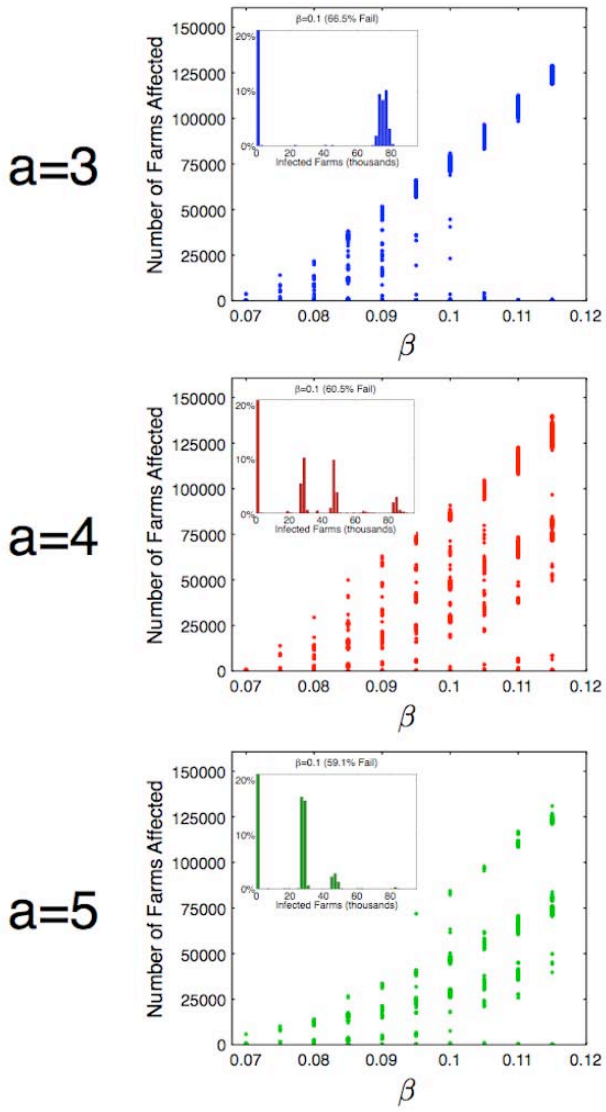

Figure 5: Severity of outbreak size for different transmission tail decays. Each point corresponds to the number of farms affected (IPs) by a complete epidemic realisation simulated using the FSR method. The distribution of outbreak sizes was multi-modal for finite mean transmission kernels as defined by (14) (*middle, bottom*). Each band of outbreak severity represented those epidemics which either failed to establish (clustered around zero farms) or were successful in invading at one or more high-risk US cattle farming regions, clustered according to which regions were invaded. The distribution of outbreak sizes for the heavy-tailed kernel K_3 was strongly bi-modal as infectious intensity β increased (*left*). For better visualisation a histogram of epidemic severities for infectious intensity $\beta = 0.1$ is given for each kernel (*insets*).

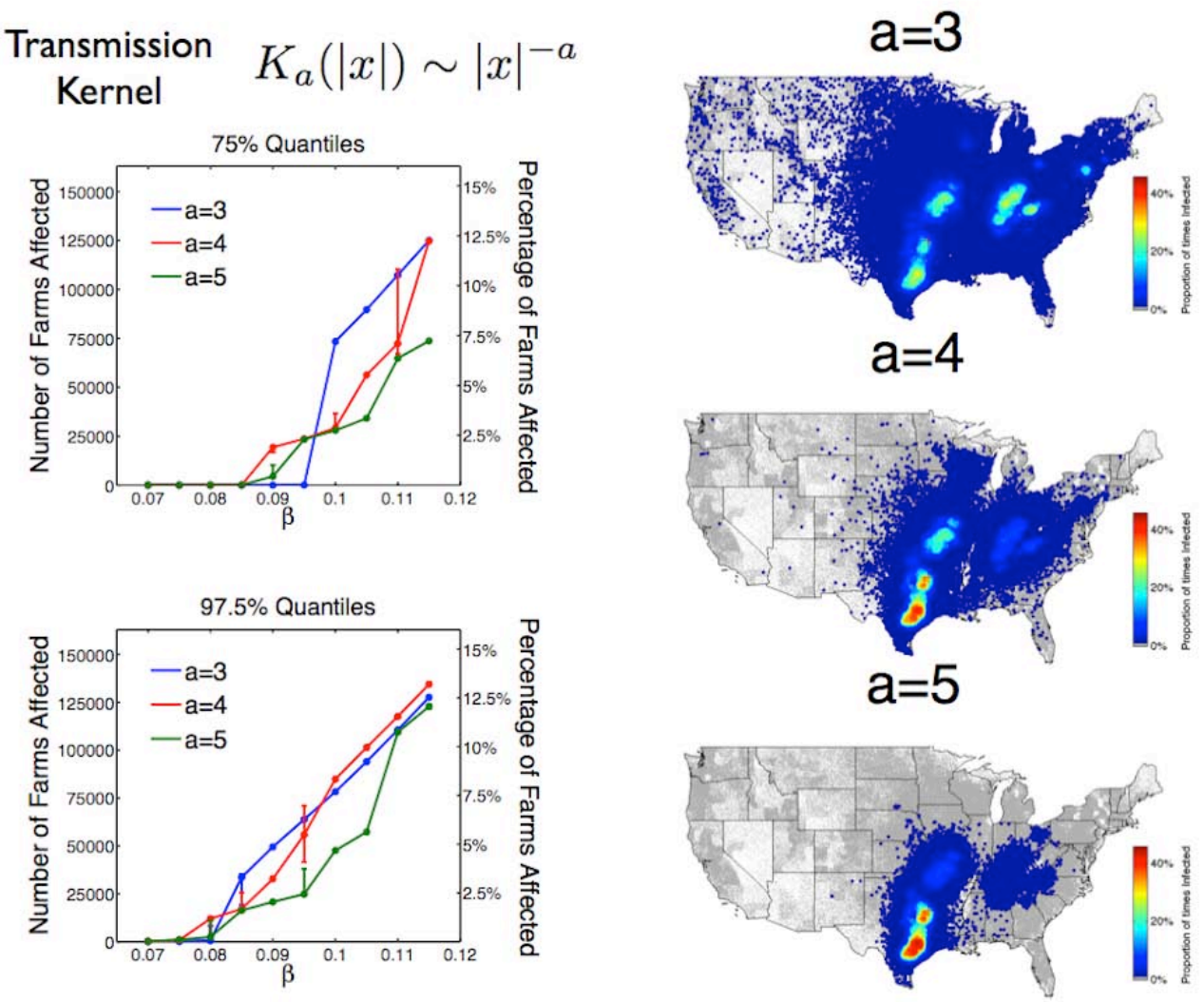

Figure 6: Quantiles and spatial distributions of disease affected farms for varying transmission tail decays. Each 75% and 97.5% quantile (*left*) was calculated from the random distribution of outbreak sizes for each infectious intensity β, 95% confidence intervals were constructed using bias corrected bootstrapping. The spatial distributions (*right*) represent farm locations as points colour coded according to their frequency of becoming infected over a number of simulations. In each case the epidemic was initiated by a single farm in Franklin county, Texas (red cross, *right*), the spatial distributions (*right*) were generated using infectious intensity $\beta = 0.1$. All statistics were calculated using 1000 FSR simulation replicates. Epidemics with the finite mean dispersal range kernels, as defined by (14), K_4 and K_5 recruited IPs most strongly in Texas. Other regions at significant risk, in decreasing order, were the central plains, the Ohio river basin and south-eastern Pennsylvania. Epidemics with heavy-tailed transmission kernel K_3 had comparatively more evenly dispersed IPs. The risk of infection for farms in areas of high cattle farm density in eastern USA didn't decrease strongly with distance from the initial source IP.

Supporting information: A Fast Spectral Method for Spatial and Stochastic Epidemic Simulation

Samuel P. C. Brand, Michael J. Tildesley, Matthew J. Keeling

1 Theoretical Basis for Fast Spectral Simulation

Let $e = (e(t), t = 0, 1, 2, \ldots; e(t) \in \{S, I, R\}^N))$ be a full trajectory of a discrete time epidemic spreading amongst the spatial metapopulation defined in the main text. We can consider both the probability measure $\mathbb{P}^{dir}(e)$ for epidemic trajectories consistent with forces of infection calculated at each time step using direct summation ($\lambda_i(t)$) and the probability measure $\mathbb{P}^{FSR}(e)$ consistent with calculating forces of infection at each time step using FSR ($\lambda_{PS}^{M,\epsilon}(x_i, t)$). By comparing the likelihood of observing e (see equation (20) of main text) for both $\mathbb{P}^{dir}$ and $\mathbb{P}^{FSR}$ we can show that if $\lambda_{PS}^{M,\epsilon}(x_i, t) \to \lambda_i(t)$ for all possible disease configurations $\{S, I, R\}^N$ then we have $\mathbb{P}^{FSR} \to \mathbb{P}^{dir}$ in the total variation metric for probability measures. For related spatial epidemic models in continuous time we can consider relative likelihoods between probability densities. Unfortunately the considerations above fail to give a sensible rate of convergence for $\mathbb{P}^{FSR} \to \mathbb{P}^{dir}$. We postulate that if the error in force of infection $|\lambda_{PS}^{M,\epsilon}(x_i, t) \to \lambda_i(t)|$ is small, then the probability of various events of interest according to $\mathbb{P}^{FSR}$ should be close to their 'true' probabilities.

Spectral versus Pseudo-spectral projection

In this subsection we review elements of the standard theory of spectral approximations to periodic functions, for example see [1] for background on spectral theory as applied to deterministic processes (PDEs) and [2] for a general introduction to discrete transforms using orthogonal basis functions. We make explicit the difference between 'true' spectral methods based on functional representation in terms of a weighted sum over a finite set of basis wave functions and the pseudo-spectral method that makes use of efficient summation over a defined collocation grid.

We consider all functions $f \in \mathcal{C}^1$ on $I_l^d = [-l/2, l/2]^d$ to be l-periodically extended to $\mathbb{R}^d$, i.e. $f(x + l\boldsymbol{n}) = f(x),\ \forall x \in I_l^d,\ \forall \boldsymbol{n} \in \mathbb{Z}^d$. In the context of the epidemic this is equivalent to imposing periodic boundary conditions on the dynamics. The requirement for periodic boundary conditions can be effectively relaxed using zero padding at the boundaries hence we do not consider this a significant restriction.

It is well known that l-periodically extended functions $f \in \mathcal{C}^1$ have a Fourier series representation, in particular

$$\lambda(x, t) \sim \frac{1}{l^d} \sum_{\omega \in \mathbb{Z}^d} \hat{\lambda}(\omega, t) e^{2\pi i \omega \cdot x / l}. \tag{1}$$

Where for each $\omega \in \mathbb{Z}^d$, the *Fourier coefficients*: $\hat{\lambda}(\omega, t)$ are defined as,

$$\hat{\lambda}(\omega, t) = \int_{I_l^d} \lambda(x, t) e^{-2\pi i \omega \cdot x / l} dx. \tag{2}$$

The relationship $\sim$ indicates uniform convergence on $\mathbb{R}^d$ as the number of wave-numbers grows to infinity, subsequently we shall use $=$ without confusion since we only consider force of infection fields with continuous first derivatives. Equation (1) indicates that the set of plane waves $\{e^{2\pi i \omega \cdot x / l}\}_{\omega \in \mathbb{Z}^d}$ form a basis for the vector space of l-periodic $\mathcal{C}^1$ functions. Note that the definition above differs from the one used in the main work. Definition (2) is the 'true' Fourier coefficient used in constructing spectral approximations to periodic functions, the Fourier coefficient calculated via FFT is a quadrature approximation to the integral in (2). We have adopted the notation ω for the spatial frequency of the time-invariant basis set of plane waves, rather than the more common k in order to avoid confusion with the notation for the transmission kernel K. For each plane wave, ω is the d-dimensional vector of spatial frequency, or *wave-vector*, for the wave in each standard Euclidean dimension.

Since this basis set is infinite in size we truncate and only use $M < \infty$ plane waves, with associated Fourier coefficients, to estimate the force of infection field, λ,

$$\lambda(x,t) \approx \lambda_S^M(x,t) = \frac{1}{l^d} \sum_{\omega \in \Omega_M^d} \hat{\lambda}(\omega,t) e^{2\pi i \omega \cdot x/l}. \tag{3}$$

The sum is over the set

$$\Omega_M^d = \{\omega = (\omega_1, \ldots, \omega_d) \in \mathbb{Z}^d \big| -m/2 \leq \omega_i \leq m/2 - 1 \ i = 1, \ldots, d\}, \tag{4}$$

with $m^d = M$. It is convenient to restrict to cases where m is even. We call this estimate, λ_S^M, the *spectral projection* of the force of infection field. The projection is onto the subspace of the square integrable functions on I_l^d, $L^2(I_l^d)$, spanned by $\{e^{2\pi i \omega \cdot x/l}\}_{\omega \in \Omega_M^d}$.

As seen in the main text the force of infection field can be represented as a convolution between the transmission kernel (K) and the image of infecteds (f_I),

$$\lambda(x,t) = K * f_I(x,t) = \int_{I_l^d} K(x-y) f_I(y,t) dy. \tag{5}$$

The representation as a convolution is very convenient for our analysis, since the Fourier coefficients $\hat{\lambda}$ are simply the the product of the Fourier coefficients of the transmission kernel $\hat{K}$ and the image of infecteds $\hat{f}_I$. This can be seen by applying definition (2) and the Fourier decomposition of K and f_I,

$$\begin{aligned}
\hat{\lambda}(\omega,t) &= \int_{I_l^d} K * f_I(x,t) e^{-2\pi i x \cdot \omega/l} dx \\
&= \int_{I_l^d} \int_{I_l^d} K(x-y) f_I(y,t) e^{-2\pi i x \cdot \omega/l} \ dy dx \\
&= \frac{1}{l^{2d}} \int_{I_l^d} \int_{I_l^d} \sum_{\omega' \in \mathbb{Z}^d} \sum_{\omega'' \in \mathbb{Z}^d} \hat{K}(\omega') \hat{f}_I(\omega'',t) e^{2\pi i y \cdot (\omega'' - \omega')/l} e^{2\pi i x \cdot (\omega' - \omega)/l} \ dy dx \\
&= \hat{K}(\omega) \hat{f}_I(\omega,t).
\end{aligned} \tag{6}$$

The final line is due to using the orthogonality of the plane waves,

$$\int_{I_l^d} e^{2\pi i (\omega - \omega') \cdot x/l} dx = l^d \delta_{\omega,\omega'}. \tag{7}$$

Equation (6) is the basis of the fast spectral rate recalculation method; it splits the time invariant and time varying parts of the force of infection field in the spatial frequency domain.

The fastest method for calculating the Fourier coefficients required for the projection approximation is by using the fast (discrete) Fourier transform (FFT) algorithm, which scales in computational complexity as $\mathcal{O}(M \log M)$ for M Fourier coefficients. The discrete transform approximates the integral (2) using sum of samples of λ at regular intervals in I_l^d. To this end we introduce a regular grid on I_l^d of separation Δx, $\Phi_{\Delta x}^{l,d}$. By varying Δx we can restrict the grid to size M, but we always choose Δx such that

$$l = m \Delta x.$$

Due to this we fix $M = m^d$ and hence,

$$\Phi_{\Delta x}^{l,d} = \{\boldsymbol{i} = (i_1, \ldots, i_d)\Delta x \mid (i_1, \ldots, i_d) \in \mathbb{Z}^d, \ 0 \leq i_j < m \ j = 1, \ldots, d\}. \tag{8}$$

The grid-points are the *collocation* points for the discrete transformation. We recall that the quadrature rules for FFT and inverse fast Fourier transform (IFFT) are respectively,

$$F\big[\lambda\big](k,t) = \tilde{\lambda}(\omega,t) = (\Delta x)^d \sum_{\boldsymbol{i} \in \Phi_{\Delta x}^{l,d}} \lambda(\boldsymbol{i},t) e^{-2\pi i (\boldsymbol{i}/\Delta x) \cdot \omega/m}, \qquad \omega \in \Omega_M^d \tag{9}$$

$$F^{-1}\big[\tilde{\lambda}\big](\boldsymbol{i},t) = \frac{1}{(m\Delta x)^d} \sum_{\omega \in \Omega_M^d} \tilde{\lambda}(k,t) e^{2\pi i (\boldsymbol{i}/\Delta x) \cdot \omega/m}, \qquad \boldsymbol{i} \in \Phi_{\Delta x}^{l,d}. \tag{10}$$

The definition above is not completely standard, it is more common in the literature not to include the factor $(\Delta x)^d$. However, when subsequently we consider products of FFT coefficients the factor $(\Delta x)^d$ becomes important.

Using Fourier coefficients estimated from a discrete quadrature rule we define the *pseudo-spectral* (discrete) projection of the force of infection field,

$$\begin{aligned} \lambda^M_{PS}(\boldsymbol{i},t) &= \frac{1}{l^d}\sum_{\omega\in\Omega^d_M}\tilde{\lambda}(\omega,t)e^{2\pi i\omega\cdot\boldsymbol{i}/l} \\ &= \frac{1}{l^d}\sum_{\omega\in\Omega^d_M}\tilde{K}(\omega)\tilde{f}_I(\omega,t)e^{2\pi i\omega\cdot\boldsymbol{i}/l} \end{aligned} \tag{11}$$

This projection onto the grid $\Phi^{l,d}_{\Delta x}$ is the approximation to the force of infection field (λ) used in this work.

Gaussian approximation and the Pseudo-Spectral Projection as a Convolution sum

One potential difficulty is that although in theory a well-defined Fourier series exists for f_I, the numerical performance of the discrete transform FFT is very poor in this situation. Essentially, the delta distributions in the infection image can be expressed as,

$$\delta(\boldsymbol{i}-x) = \frac{1}{l^d}\sum_{\omega\in\mathbb{Z}^d} e^{2\pi i\omega\cdot(\boldsymbol{i}-x)/l}. \tag{12}$$

However any finite truncation of this sum does not provide a good approximation to the delta distribution. We resolve with this problem by introducing *blurred images*, where the delta distributions in the image definition are replaced by tight Gaussians of width ϵ (>0),

$$\delta_\epsilon(x) = \frac{1}{(2\pi\epsilon^2)^{d/2}}e^{-\frac{-|x|^2}{2\epsilon^2}}. \tag{13}$$

This approximation is justified by the convergence,

$$\epsilon\to 0_+ \Rightarrow \delta_\epsilon(x-x_i)\to\delta(x-x_i).$$

Where $\to$ is weak convergence in distribution.

The image of infecteds with delta distributions approximated by Gaussians is denoted

$$\begin{aligned} f^\epsilon_I(x,t) &= \sum_{j=1}^N \delta_\epsilon(x-x_i)I_j(t) \\ &= \frac{1}{l^d}\sum_{\omega\in\mathbb{Z}^d}\sum_{j=1}^N I_j(t)e^{-2\pi^2\omega^2\epsilon^2/l^2}e^{2\pi i\omega\cdot(x-x_j)/l} \end{aligned} \tag{14}$$

Note that the effect of the Gaussian approximation on the image of infecteds Fourier representation is to decrease each Fourier coefficient by a factor $e^{-2\pi^2\omega^2\epsilon^2/l^2}$. This causes the sum over wave vectors to converge, by filtering out the effect of the high frequency waves. The source of the Gaussian factor is due to Gaussians in the spatial domain being represented as Gaussians in the frequency domain with inverted width. For $\epsilon \ll l$,

$$\hat{\delta}_\epsilon(\omega) = \int_{I^d_l}\delta_\epsilon(x)e^{-2\pi i\omega\cdot x}dx = e^{-2\pi^2\omega^2\epsilon^2/l^2}. \tag{15}$$

This identity is easily calculated by using standard completing of the square in the exponent of the exponential function and using that δ_ϵ is normalised.

Since f^ϵ_I is a well defined bounded function on I^d_l we can consider a sum approximation to the convolution integral form for the force of infection field,

$$\lambda(\boldsymbol{i},t) = K * f_I(\boldsymbol{i},t) \approx K * f^\epsilon_I(\boldsymbol{i},t) \approx (\Delta x)^d \sum_{\boldsymbol{j}\in\Phi^{l,d}_{\Delta x}} K(\{\boldsymbol{i}-\boldsymbol{j}\}_l)f^\epsilon_I(\boldsymbol{j}). \tag{16}$$

Where,

$$K(\{\boldsymbol{i}-\boldsymbol{j}\}_l) = K((\boldsymbol{i}-\boldsymbol{j})^*) + \sum_{\boldsymbol{n}\in\mathbb{Z}^d} K((\boldsymbol{i}-\boldsymbol{j})^* + \boldsymbol{n}l). \tag{17}$$

$(\boldsymbol{i}-\boldsymbol{j})^*$ denotes the shortest euclidean distance between grid points $\boldsymbol{i}$ and $\boldsymbol{j}$ on the periodic domain I_l^d, which possibly may not coincide with $|\boldsymbol{i}-\boldsymbol{j}|$. The extra contribution is also due to periodicity - that the distribution of infected habitats creates an infectious potential on a point due to the shortest range interaction, and then that range plus an extra revolution around the space and so on. This is obviously not an effect of interest in spatial modelling with application; it is in fact is negligible due to restricting to transmission kernels that are sufficiently short range compared to the space that only the shortest range interactions contribute.

The natural approximation of the force of infection is, in fact, identical to the pseudo-spectral projection of the force of infection field using Gaussian approximations for the delta distributions of habitat locations. Applying definition (9) to the pseudo-spectral projection (11) with the Fourier coefficients of the image of infected replaced by their 'blurry' Gaussian approximation gives that,

$$\begin{aligned}
\lambda(\boldsymbol{i},t) &\approx (\Delta x)^d \sum_{\boldsymbol{j}\in\Phi_{\Delta x}^{l,d}} K(\{\boldsymbol{i}-\boldsymbol{j}\}_l) f_I^\epsilon(\boldsymbol{j}) \\
&= \frac{(\Delta x)^d}{m^{2d}(\Delta x)^{2d}} \sum_{\boldsymbol{j}\in\Phi_{\Delta x}^{l,d}} \sum_{\omega\in\Omega_M^d} \sum_{\omega'\in\Omega_M^d} \tilde{K}(\omega)\tilde{f}_I^\epsilon(\omega',t) e^{2\pi i[\boldsymbol{i}\cdot\omega + \boldsymbol{j}\cdot(\omega'-\omega)]/(m\Delta x)} \\
&= \frac{1}{l^d} \sum_{\omega\in\Omega_M^d} \tilde{K}(\omega)\tilde{f}_I^\epsilon(\omega,t) e^{2\pi i\omega\cdot\boldsymbol{i}/l} \\
&= \lambda_{PS}^{M,\epsilon}(\boldsymbol{i},t), \qquad \boldsymbol{i}\in\Phi_{\Delta x}^{l,d},\ t\in\mathbb{R}_+.
\end{aligned} \tag{18}$$

Where I have used that for $\boldsymbol{i}\in\Phi_{\Delta x}^{l,d}$, $\boldsymbol{i}/\Delta x\in\mathbb{Z}^d$, by construction. Now, by considering mth roots of unity we get the analogous discrete orthogonality relationship to (7),

$$\sum_{\boldsymbol{j}\in\Phi_{\Delta x}^{l,d}} e^{2\pi i(\boldsymbol{j}/\Delta x)\cdot(\omega'-\omega)/m} = m^d\delta_{\omega',\omega+mp}, \qquad p\in\mathbb{Z}^d. \tag{19}$$

Note that this orthogonality relation is periodic, it does not distinguish between the equivalence classes of the form $[\omega]_m = \{\omega + m\boldsymbol{n}|\boldsymbol{n}\in\mathbb{Z}^d\}$. It is the discrete projection $\lambda_{PS}^{M,\epsilon}$ that we can solve for each point $\boldsymbol{i}\in\Phi_{\Delta x}^{l,d}$ with computation cost $\mathcal{O}(M\ln M)$ using the FFT convolution solution as described in the main work.

A final consideration is choice of M, which in turn determines Δx. FFT algorithms operate via the factorisation of M, with greater operational speed if M has a factorisation into small primes. Hence, having tuned parameters for acceptable error it is better to pick M such that it has a factorisation into a product of powers of $2, 3, 5$. This typically constitutes a small modification of Δx. Where possible we have chosen M as a power of 2 for maximum efficiency of calculation.

Convergence of Pseudo-Spectral Approximation

In this section we discuss the interplay between choosing grid separation Δx and Gaussian width, ϵ, in terms of an upper bound on the error in the force of infection due to using FSR. In following sections we will justify the upper bound (20). For smooth transmission kernels, K, we have that for any epidemic state $X(t)$ a upper bound on the uniform error (the worst error anywhere in I_l) between the true (λ) and estimated ($\lambda_{PS}^{M,\epsilon}$) force of infection field,

$$\begin{aligned}
\|\lambda_{PS}^{M,\epsilon} - \lambda\|_\infty &\leq \Psi\|\lambda_S^M\|_\infty + \frac{\epsilon^2}{2}\|\Delta\lambda_S^M\|_\infty + Ce^{-\xi M} + \mathcal{O}(\epsilon^4) \\
&\approx \Psi\|\lambda\|_\infty + \frac{\epsilon^2}{2}\|\Delta\lambda\|_\infty + \mathcal{O}(\epsilon^4)
\end{aligned} \tag{20}$$

Where $\|f\|_\infty = \sup_{x\in I_l^d}\{|f(x)|\}$ is a uniform norm on the spatial variables, and can therefore vary with time. The exponentially decaying term, with $C>0$ and $\xi>0$ constants, gives the uniform error due to the 'true' spectral approximation of the force of infection field (λ_S^M) using a projection of M plane waves. In practise this is the least

significant error term, and the approximation in (20) is valid for large grid sizes. Δ is the Laplacian operator for the spatial variables, and Ψ is an error factor due to using the discrete grid $\Phi^l_{\Delta x}$ to approximate the Fourier coefficients. $\Psi(r)$ is an increasing function in the ratio of Gaussian width to grid width,

$$r = \Delta x/\epsilon, \tag{21}$$

with

$$\Psi(r) \to 0, \qquad \text{as } r \to 0. \tag{22}$$

Equations (20) and (22) provide several key insights into the FSR method:

- Smooth transmission kernels, K, lead to the small uniform norms in (20), and hence greater expected accuracy for the FSR method. In particular the transmission kernels considered in the main work were each parametrised by a length scale L. As $L \to \infty$ then the force of infection everywhere converges to its mean-field limit $\|\lambda(t)\|_\infty \to \beta I(t)/l^d$ where $I(t)$ is the number of infected habitats at time t and β is the magnitude of the transmission kernel; similarly $\|\Delta\lambda\|_\infty \to 0$. Therefore for large L kernels the grid to Gaussian width ratio r can be made small on a coarse grid by using wide gaussians ($\epsilon \gg \Delta x$) without loss of accuracy.

- For any $\epsilon > 0$,

$$\lim_{\Delta x \to 0} \|\lambda^{M,\epsilon}_{PS} - \lambda\|_\infty \leq \frac{\epsilon^2}{2}\|\Delta\lambda\|_\infty + \mathcal{O}(\epsilon^4). \tag{23}$$

  Therefore, the uniform error (20) can be set arbitrarily small by reducing both Δx and ϵ.

- As we increase the width of the space we consider (l) the uniform norms in (20) depend on how the habitats are distributed since they represent the maximum rate of infection anywhere in I_l for the disease state $X(t)$. For randomly distributed habitats this maximum rate will grow very slowly with l.

- For a given collocation grid with $\Delta x > 0$, there exists an error trade-off between the two extremes of choosing a tight Gaussian ($\epsilon \ll \Delta x$), which can lead to large values of Ψ and choosing a disperse Gaussian ($\epsilon \gg \Delta x$) when the ϵ^2 term dominates.

- The upper bound (20) is itself upper bounded by the case where all habitats share an identical spatial location. For $I(t)$ infectious habitats this gives,

$$\|\lambda^{M,\epsilon}_{PS} - \lambda\|_\infty \leq I(t)\big[\Psi\|K\|_\infty + \frac{\epsilon^2}{2}\|\Delta K\|_\infty\big] + Ce^{-\alpha M} + \mathcal{O}(\epsilon^4). \tag{24}$$

  Which suggests that ϵ could be chosen so as to minimise,

$$\Psi\|K\|_\infty + \frac{\epsilon^2}{2}\|\Delta K\|_\infty. \tag{25}$$

  Which is an expression independent of the distribution of habitats. On the other hand choosing ϵ as to minimise (25) is not necessarily the optimal or even simplest solution. In the main work we used a corrected kernel spectrum with the goal of compensating for the effect of Gaussian blurring on the spectrum of the force of infection field. Therefore error due to using corrected spectrum FSR has a weaker dependence on choosing ϵ as too great. This consideration motivates choosing ϵ as sufficiently great that a unit Gaussian has unit mass on the approximation grid ($\tilde{\delta}_\epsilon(0) \approx 1$) but no larger.

Derivation of Error Upper Bound

We turn to the derivation of the upper bound (20). The upper bound is for FSR without Kernel correction, in subsequent sections we then demonstrate a further improvement in accuracy due to using corrected spectrum FSR. There are three sources of error in the approximation scheme $\lambda \approx \lambda^{M,\epsilon}_{PS}$.

- *Aliasing error* due to FFT being a discrete transformation with a quadrature on discrete spatial points replacing an integral on continuous space.

- *Projection error* due to projecting K and f^ϵ_I onto the subspace $L^2_M(I^d_l)$ constructed using $M < \infty$ plane waves.

- The approximation of delta distributions by Gaussians.

The smoothness of the force of infection field, λ, is guaranteed by the smoothness of the transmission kernel. This in turn guarantees the existence of the spectral projection of the force of infection field (λ_S^M) and its counterpart with delta distributions replaced by approximating Gaussians,

$$\lambda_S^{M,\epsilon}(x,t) = \frac{1}{l^d} \sum_{\omega \in \Omega_M^d} \hat{K}(\omega) \hat{f}_I^{\epsilon}(\omega,t) e^{2\pi i \omega \cdot x/l} \tag{26}$$

We can decompose the uniform error between the true force of infection field and its pseudo-spectral projection using Gaussian approximation into the useful upper bound,

$$\|\lambda_{PS}^{M,\epsilon} - \lambda\|_\infty \leq \|\lambda_{PS}^{M,\epsilon} - \lambda_S^{M,\epsilon}\|_\infty + \|\lambda_S^{M,\epsilon} - \lambda_S^M\|_\infty + \|\lambda_S^M - \lambda\|_\infty. \tag{27}$$

Each term on the right hand side of above is respectively, the aliasing error, the Gaussian approximation error and the spectral error. We consider each case separately. The projection error is given by a standard result, however the error analysis for the error due to aliasing and Gaussian approximation is more involved. We make the general point that the smaller ϵ the better for the Gaussian approximation, but the less support $\lambda_{PS}^{M,\epsilon}$ has on $\Phi_{\Delta x}^{l,d}$ and hence, for fixed Δx, the worse the aliasing error.

Projection Error:
Due to the smoothness of the force of infection field, it is well known [1] we have convergence as $M \to \infty$ for the spectral projection λ_S^M to λ. Moreover, the rate of convergence is exponential,

$$\|\lambda_S^M(\cdot,t) - \lambda(\cdot,t)\|_\infty \sim Ce^{-\alpha M}, \tag{28}$$

for some $C > 0$ and $\alpha > 0$ dependent on the smoothness of λ. In practise this is the least significant term in (27).

Aliasing Error:
Recall that in each dimension we implement FFT on $m = (l/\Delta x)$ discrete frequencies, i.e. $M = (l/\Delta x)^d = m^d$. A classic manipulation is the decomposition using (1) and (9) [3, 2],

$$\begin{aligned}
\tilde{\lambda}(\omega,t) &= (\Delta x)^d \sum_{\boldsymbol{j} \in \Phi_{\Delta x}^{l,d}} \lambda(\boldsymbol{j}) e^{-2\pi i \omega \cdot (\boldsymbol{j}/\Delta x)/m} \\
&= \frac{(\Delta x)^d}{l^d} \sum_{\boldsymbol{j} \in \Phi_{\Delta x}^{l,d}} \sum_{\omega' \in \mathbb{Z}^d} \hat{\lambda}(\omega',t) e^{2\pi i \omega' \cdot (\boldsymbol{j}/\Delta x)/m} e^{-2\pi i \omega \cdot (\boldsymbol{j}/\Delta x)/m} \\
&= m^d \frac{(\Delta x)^d}{l^d} \sum_{\omega' \in \mathbb{Z}^d} \hat{\lambda}(\omega',t) \delta_{\omega', \omega + mp}, \qquad p \in \mathbb{Z}^d, \\
&= \hat{\lambda}(\omega,t) + \sum_{p \neq 0} \hat{\lambda}(\omega + mp).
\end{aligned} \tag{29}$$

Where $\hat{f}(\omega)$ is the Fourier coefficient for f at discrete frequency $\omega \in \mathbb{Z}^d$. This relates the 'true' Fourier coefficient to the FFT estimate. The second term in the sum is the aliasing error induced by the indistinguishability of modes within the equivalence classes $[\omega]_m$.

We make the reasonable assumption that the transmission kernel has a known Fourier series $\hat{K}$, or has negligible aliasing error. We analysis the aliasing error dependence on grid width (Δx) and Gaussian approximation width (ϵ) through the ratio,

$$r = \frac{\Delta x}{\epsilon}. \tag{30}$$

We will find that as the grid width becomes significantly less than the width of the Gaussian approximation ($r \to 0$) the aliasing error becomes negligible.

Using equation (29) the aliasing error, for a given state $X(t)$ and $x \in I_l^d$, can be written as,

$$\begin{aligned} |(\lambda_{PS}^{M,\epsilon} - \lambda_S^{M,\epsilon})(x,t)| &= \frac{1}{l^d}\Big| \sum_{\omega \in \Omega_M^d} \hat{K}(\omega)(\tilde{f}_I^\epsilon(\omega) - \hat{f}_I^\epsilon(\omega))e^{2\pi i\omega\cdot x/l}\Big| \\ &= \frac{1}{l^d}\Big| \sum_{\omega \in \Omega_M^d} \hat{K}(\omega)\sum_{j=1}^N I_j(t)e^{2\pi i\omega\cdot(x-x_j)/l}\sum_{p\neq 0} e^{-2\pi imp\cdot(\frac{x_j}{\Delta x})/m}e^{-2\pi^2(\omega+mp)^2/r^2m^2}\Big| \end{aligned} \tag{31}$$

We emphasis that the Gaussian approximation to the delta distribution was necessary for good numerical performance since the sum $\sum_{p\neq 0} e^{-2\pi ip\cdot(\frac{x_j}{\Delta x})}$ does not converge, causing significant aliasing error in the pseudo-spectral approach to force of infection calculation with $\epsilon = 0$, however big M is allowed to become. However, the sum $\sum_{p\neq 0} e^{-2\pi^2(\omega+mp)^2/r^2m^2}$ converges for all $r > 0$.

An obvious progression from (31) is to use the Cauchy-Schwarz inequality, however this leads to rather crude estimates for the aliasing error for a given choice of Δx, ϵ. Instead, we exploit the special structure of the force of infection field's spectral representation. It is convenient to define an alias function for each habitat,

$$\alpha_j^\epsilon(x) = \frac{1}{l^d}\sum_{\omega\in\mathbb{Z}^d}\sum_{p\neq 0} e^{-2\pi imp\cdot(\frac{x_j}{\Delta x})/m}e^{-2\pi^2(\omega+mp)^2/r^2m^2}e^{2\pi i\omega\cdot x/l}, \qquad x \in I_l^d,\ j = 1,\dots,N. \tag{32}$$

We note that under variation of habitat location, x_j, α_j is everywhere maximised by choosing x_j on the grid; that is that $(x_j/\Delta x) \in \mathbb{Z}^d$. This gives the dominant alias function,

$$\alpha^\epsilon(x) = \frac{1}{l^d}\sum_{\omega\in\mathbb{Z}^d}\sum_{p\neq 0} e^{-2\pi^2(\omega+mp)^2/r^2m^2}e^{2\pi i\omega\cdot x/l}. \tag{33}$$

The alias function α^ϵ gives the x dependent difference between the pseudo-spectral and true spectral approximations of a d-dimensional zero-centred Gaussian of width ϵ. Numerical investigation suggests that α^ϵ is a positive function. We note from (31) that the difference between the pseudo-spectral and true spectral approximations for the force of infection field can be written in the convolution form, where the ϵ dependence is subsumed into the alias function,

$$\begin{aligned} |(\lambda_{PS}^{M,\epsilon} - \lambda_S^{M,\epsilon})(x,t)| &= |\sum_{j=1}^N I_j(t)(K*\alpha_j^\epsilon)_S^M(x-x_j)| \\ &\leq |\sum_{j=1}^N I_j(t)(K*\alpha^\epsilon)_S^M(x-x_j)| \\ &= |[(f_I*K)*\alpha^\epsilon]_S^M(x,t)| \\ &= |(\lambda*\alpha^\epsilon)_S^M(x,t)|. \end{aligned} \tag{34}$$

Combining (34) with Young's inequality for convolutions gives the inequality,

$$\|(\lambda_{PS}^{M,\epsilon} - \lambda_S^{M,\epsilon})\|_\infty \leq \|\lambda_S^M\|_\infty\|(\alpha^\epsilon)_S^M\|_1. \tag{35}$$

Using the positivity of α^ϵ gives,

$$\|(\alpha^\epsilon)_S^M\|_1 = \sum_{p\neq 0} e^{-2\pi^2p^2/r^2} = \sum_{p\in\mathbb{Z}^d} e^{-2\pi^2p^2/r^2} - 1 = \Big(\sum_{n\in\mathbb{Z}} e^{-2\pi^2n^2/r^2}\Big)^d - 1 \tag{36}$$

We recall the standard result of analysis that for non-negative monotonically decreasing functions f,

$$\sum_{n=N}^M f(n) \leq f(N) + \int_N^M f(x)dx.$$

We also note that $f(x) = e^{-2\pi^2(x-\omega_i^*/m)^2/r^2}$ is monotonically decreasing on $[0,\infty)$. For each sum in the product term in (36) we have, via standard sum splitting and change of variable,

$$\begin{aligned} \sum_{n=-\infty}^{\infty} e^{-2\pi^2n^2/r^2} &= \sum_{j=0}^{\infty} e^{-2\pi^2j^2/r^2} + \sum_{l=1}^{\infty} e^{-2\pi^2l^2/r^2} \\ &\leq 1 + e^{-2\pi^2/r^2} + \int_0^\infty e^{-2\pi^2x^2/r^2}dx + \int_1^\infty e^{-2\pi^2x^2/r^2}dx. \end{aligned} \tag{37}$$

The integrals in (37) have unnormalised Gaussian probability density functions as their integrand. This permits the following inequality,

$$\int_0^\infty e^{-2\pi^2x^2/r^2}dx + \int_1^\infty e^{-2\pi^2x^2/r^2}dx = \frac{r}{\sqrt{2\pi}}\Big[1 - \frac{\sqrt{2\pi}}{r}\int_0^1 e^{-2\pi^2x^2/r^2}dx\Big]$$
$$= \frac{r}{\sqrt{2\pi}}\mathbb{P}(Y \geq 1 \ \vee \ Y \leq 0). \tag{38}$$

Where the random variable $Y \sim \mathcal{N}(0, r^2/4\pi^2)$. We can use Chebyshev's inequality and the symmetry of the Gaussian distribution to bound the probability above in terms of r.

$$\mathbb{P}(Y \geq 1 \ \vee \ Y \leq 0) = 1/2 + \mathbb{P}(Y \geq 1) = 1/2(1 + \mathbb{P}(|Y| \geq 1))$$
$$\leq 1/2\Big(1 + \frac{r^2}{4\pi^2}\Big). \tag{39}$$

Introducing (37), (38) and (39) into (36) gives,

$$\sum_{p\in\mathbb{Z}^d} e^{-2\pi^2p^2/r^2} - 1 \leq \prod_{i=1}^d \Big(1 + e^{-2\pi^2/r^2} + \frac{r^3 + 4\pi^2r}{2(2\pi)^{5/2}}\Big) - 1 \tag{40}$$

For compactness of representation we now write,

$$\psi = 1 + e^{-2\pi^2/r^2} + \frac{r^3 + 4\pi^2r}{2(2\pi)^{5/2}}.$$

Introducing this estimate into equation (35) gives an upper bound for the error due to aliasing,

$$\|\lambda_{PS}^{M,\epsilon} - \lambda_S^{M,\epsilon}\|_\infty \quad \leq \quad (\psi^d - 1)\|\lambda_S^M\|_\infty \tag{41}$$

The error factor $\Psi(r)$ in upper bound (20) is,

$$\Psi(r) = (\psi(r)^d - 1) \to_{r\to 0} 0. \tag{42}$$

Gaussian Approximation Error:
For the uniform Gaussian approximation error we can exploit the definition of the exponential function and use a standard result for spectral representation of derivatives of smooth functions, f,

$$\Delta^k f = \frac{1}{l^d}\sum_{\omega\in\mathbb{Z}^d} \frac{(-4\pi^2\omega^2)^k}{l^{2k}}\hat{f}(\omega)e^{2\pi i\omega\cdot x/l}.$$

Where Δ^k is the k-fold operator mapping on suitably regular functions f of the Laplacian ($\Delta = \sum_{i=1}^d \frac{\partial^2}{\partial x_{(i)}^2}$ where $x = (x_{(1)}, \ldots, x_{(d)})$),

$$\Delta^k f = \Delta(\Delta^{k-1}f) = \ldots = \Delta(\Delta(\ldots\Delta(\Delta f)\ldots).$$

Hence, by using the definition of the spectral projection with Gaussian approximation we can write,

$$\begin{aligned}
\|\lambda_S^{M,\epsilon} - \lambda_S^M\|_\infty &= \Big|\frac{1}{l^d}\sum_{\omega\in\Omega_M^d} \hat{K}(\omega)[\hat{f}_I^\epsilon(\omega) - \hat{f}_I(\omega)]e^{2\pi i\omega\cdot x^*/l}\Big|, \qquad x^* \in \arg\max_{x\in I_l^d}\{|(\lambda_S^{M,\epsilon} - \lambda_S^M)(x,t)|\} \\
&= \Big|\frac{1}{l^d}\sum_{\omega\in\Omega_M^d} \hat{K}(\omega)\sum_{j=1}^N I_j(t)[e^{-2\pi^2\omega^2\epsilon^2/l} - 1]e^{2\pi i\omega\cdot(x^* - x_j)/l}\Big| \\
&= \Big|\frac{1}{l^d}\sum_{\omega\in\Omega_M^d} \hat{K}(\omega)\sum_{j=1}^N I_j(t)\sum_{k\geq 1}\frac{(-4\pi^2\omega^2/l^2)^k\epsilon^{2k}}{2^k k!}e^{2\pi i\omega\cdot(x^* - x_j)/l}\Big| \\
&\leq \Big\|\sum_{k\geq 1}\frac{\epsilon^{2k}}{2^k k!}\Delta^k\lambda_S^M\Big\|_\infty
\end{aligned} \tag{43}$$

In application we use the small ϵ estimate for (43),

$$\|\lambda_S^{M,\epsilon} - \lambda_S^M\|_\infty \quad \leq \quad \frac{\epsilon^2}{2}\|\Delta\lambda\|_\infty + \mathcal{O}(\epsilon^4) \tag{44}$$

Corrected Spectrum FSR

In the main work we did not use the kernel spectrum $\tilde{K}$ in order to resolve the pseudo-spectral projection of the force of infection field on the collocation grid. Instead, the corrected pseudo-spectrum,

$$\tilde{K}'(\omega) = \frac{\tilde{K}(\omega)}{\tilde{\delta}_\epsilon(\omega)}, \qquad \omega \in \Omega_M^d, \tag{45}$$

was used. The motivation for (45) is the exact relation between the spectra of λ and the blurry image of infection,

$$\hat{\lambda} = \hat{K}\hat{f}_I = \hat{K}'\hat{f}_I^\epsilon. \tag{46}$$

Hence, using corrected spectrum FSR is a computational trick to rewrite a product involving a difficult to resolve spectrum ($\hat{f}_I$) in terms of two spectra that can be readily estimated using FFT.

A diagnostic that FFT is providing a good estimate for the spectrum of the zero centred Gaussian is the mass supported on the collection grid, that is the zero-mode of the pseudo-spectrum $\tilde{\delta}_\epsilon(0)$. The mass supported on the grid should be 1 for the unit Gaussian, otherwise the Gaussian is either under-resolved, or in extreme cases as $\epsilon \to 0$ the central spike of Gaussian dominates the pseudo-spectrum. In either case poor numerical performance should be expected. Throughout the main work ϵ was chosen so that $\tilde{\delta}_\epsilon(0) \approx 1$ but no greater. This choice of ϵ has two main motivations: (i) greater values of ϵ on a given collocation grid implies a greater number of local points for each habitat and therefore increased computational burden for FSR and (ii) $\tilde{\delta}_\epsilon(\omega) \to 0$ as $|\omega| \to \infty$ faster for greater values of ϵ. This effectively limits the space of contributing wave-vectors to the projection $\lambda_{PS}^{M,\epsilon}$, where the corrected spectrum $\tilde{K}'$ is used. This would lead to poor projection error if ϵ is chosen much too great.

We now re-present the numerical performance of FSR given in the main text, with the additional comparison of uncorrected kernel FSR. The same baseline parameters were chosen ($N = 12\,100,\ \beta = 2,\ L = 3,\ \Delta x = 0.5$ with Gaussian transmission kernel) as the main text, and a numerical investigation was performed by varying grid width (Δx), transmission range (L) and number of habitats (N). Simulations using uncorrected kernel FSR each had ϵ chosen to minimise the 'worst possible' upper bound (25). For each combination of parameters considered corrected kernel FSR out performed uncorrected FSR in the sense of having a smaller error density (as defined in main text) for both supremum error and final error. For the baseline parameters the supremum error density found using uncorrected kernel FSR was 2.23×10^{-2} ($[2.12\times10^{-2}, 2.36\times10^{-2}$) compared to 6.7×10^{-3} ($[6.2\times10^{-3}, 7.3\times10^{-3}]$). The dependence of error density upon parameter variation found to be similar for uncorrected kernel FSR as for corrected kernel FSR. That is that error density was increasing with coarser grids (greater Δx), decreasing with longer range transmission (greater L) and only weakly dependent upon metapopulation size (Figure 1A-C).

The expected dynamics of infecteds for the metapopulation epidemic (averaged over 1000 simulation replicates) considered in the main work were still well estimated using uncorrected kernel FSR compared to the corrected kernel version. The worst absolute error in expected numbers of infected habitats throughout the epidemic found using uncorrected kernel FSR was 34.35 (0.32% of the metapopulation). However, this small error is still significantly greater than that found for corrected kernel FSR (figure 1D).

References

[1] Tveito A, Winther R. Introduction to Partial Differential Equations: A Computational Approach. New York; 1998. Springer.

[2] Xiu D. Numerical Methods for Stochastic Computations. A Spectral Method Approach. Princeton: Princeton University Press; 2010.

[3] Hesthaven J, Gottlieb S, Gottlieb D. Spectral methods for time-dependent problems. Cambridge; 2007. Cambridge University Press.

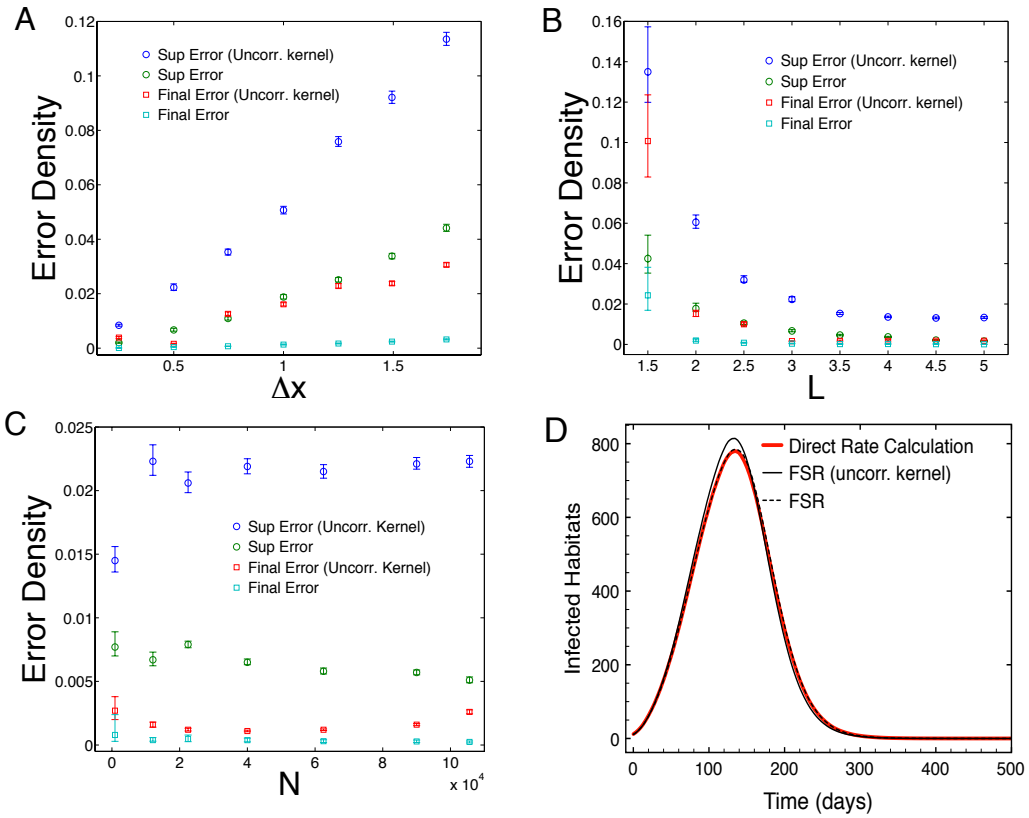

Figure 1: An error comparison between uncorrected kernel FSR and FSR using a corrected kernel spectrum. All confidence intervals are due to bias corrected 95% confidence boot-strapping. The base set of parameters was $N = 12\,100,\ \beta = 2,\ L = 3,\ \Delta x = 0.5$ with Gaussian transmission kernel. **A-C**: Varying the base parameter set in grid width (Δx), transmission range (L) and number of habitats (N). Mean supremum error density (circles) and mean final error density (squares) are shown for both uncorrected kernel FSR and the corrected kernel FSR used in the main text. For each parameter choice corrected kernel FSR had a lesser mean error density. **D**: The time varying expected number of infected habitats for the baseline parameters with 10 initial infecteds is compared to that found using uncorrected and corrected kernel FSR. The expected epidemic curve estimated using corrected kernel FSR is more accurate. Each epidemic curve was estimated using 1000 simulation replicates.